International Journal of Heat and Mass Transfer 194 (2022) 123099

Contents lists available at ScienceDirect

International Journal of Heat and Mass Transfer

journal homepage: www.elsevier.com/locate/hmt

Combined numerical and experimental studies of 21700 lithium-ion battery thermal runaway induced by different thermal abuse

Ashish V. Shelkea[a], Jonathan E.H. Buston[b], Jason Gill[b], Daniel Howard[b], Rhiannon C.E. Williams[b], Elliott Read[b], Ahmed Abaza[c], Brian Cooper[c], Philp Richards[c], Jennifer X. Wen[a,*]

[a] Warwick FIRE, School of Engineering, University of Warwick, Coventry CV4 7AL, UK
[b] The Health and Safety Executive Science and Research Centre, Harpur Hill, Buxton SK17 9JN, UK
[c] Jaguar Land Rover Limited, Abbey Road, Whitley, Coventry CV3 4LF, UK

ARTICLE INFO

Article history:
Received 14 February 2022
Revised 27 April 2022
Accepted 1 June 2022

Keywords:
Thermal runaway
Lithium-ion battery
EV-ARC tests
Decomposition reactions
Validation of CFD based predictive tools
Parametric studies

ABSTRACT

Combined numerical and experimental studies have been carried out to investigate thermal runaway (TR) of large format 21700 cylindrical lithium-ion battery (LIB) induced by different thermal abuse. Experiments were firstly conducted with the Extend Volume Accelerating Calorimetry (EV-ARC) using both the heat-wait-seek (HWS) protocol and under isothermal conditions. The kinetic parameters were derived from one of the HWS EV-ARC tests and implemented in the in-house modified computational fluid dynamics (CFD) code OpenFOAM. For the subsequent CFD simulations, the cell was treated as a 3-D block with anisotropic thermal conductivities. The model was verified by the remaining two HWS tests not used in the derivation of the kinetic parameters and validated with newly conducted isothermal EV-ARC tests. Further laboratory tests and model validation were also subsequently conducted using Kanthal wire heaters. The validated model was also used to fill the experimental gaps by predicting the onset temperature for TR in simulated EV-ARC environment, heat generation rate due to different abuse reactions, the influence of heating power and heating arrangement as well as the effect of heat dissipation on TR evolution and the implications for battery thermal management. The present study has identified the TR onset temperature of the considered 21700 LIB to be between 131 and 132 °C. The predicted heat generation rate due to the decompositions of SEI and anode were found to follow similar patterns while that from cathode increase sharply near the maximum cell surface temperature, indicating the possibility of delaying TR onset temperature by optimising the cathode material. The time to maximum cell surface temperature decreases rapidly with the increase of the heating power.

1. Introduction

Lithium-ion batteries (LIBs) are increasingly used in electric vehicles (EVs) [1]. They are also popular for grid storage applications to replace non-battery energy storage device [2]. To deliver the desired driving range for EVs, the energy density of LIBs is gradually increasing. A larger 21700 format has been adopted by some manufacturers. The increased cell size leads to larger capacity and energy density in comparison with the 18650 format [3]. However, relatively few studies have addressed the thermal behavior of 21700 cells [4–7].

LIB performance is influenced by its operational temperature [8,9]. The cell may enter thermal runaway (TR) and fail irreversibly when subjected to external heating, releasing particulate matter and flammable gases [10,11]. The propagation of TR from the original cell to the adjacent cells in battery packs and modules can escalate into serious fire incidents in EVs and LIB based energy storage facilities [12]. The consequence of such potential incidents is even higher for LIBs with high-energy density.

1.1. Knowledge gaps in experimental investigations

Previous experimental investigations of TR in cylindrical cells have been conducted with a range of heating arrangements including heating in isothermal environment either in Accelerating Rate Calorimetry (ARC) or other reactor [22–24], or the heat-wait-seek (HWS) protocol in ARC [5,25–27] as well as side-heating with plate

* Corresponding author.
E-mail address: jennifer.wen@warwick.ac.uk (J.X. Wen).

https://doi.org/10.1016/j.ijheatmasstransfer.2022.123099

Nomenclature

A_{cell}	surface area of the cell (m^2)
A_i	pre-exponential factor for the reaction (s^{-1})
c_i	normalized amount of the reactant
Cp	total heat capacity (J/KgK)
E_i	activation energy for the reaction (J/mol)
H_i	reaction heat
h_{conv}	convective heat transfer coefficient (W/m^2K)
ΔH	heat released during TR
g	gravitational acceleration
k_b	Boltzmann's constant
κ_i	rate constant of the reaction
$m_{battery}$	cell mass (g)
n	reaction order
$\dot{Q}_{exo}$	volumetric heat generated
$\dot{Q}_{SEI}$	heat due to decomposition of SEI layer (W)
$\dot{Q}_{An}$	heat due to decomposition of anode (W)
$\dot{Q}_{Ca}$	heat due to decomposition of cathode (W)
$\dot{Q}_{Mix}$	heat due to decomposition of electrolyte and other remaining materials (W)
Q_{conv}	heat source of the convection (W)
Q_{rad}	heat source of the radiation (W).
t_{ex}	exothermic time (min)
T_{ab}	final adiabatic temperature (°C)
δT_{ab}	adiabatic temperature rise (°C)
T_{cell}	surface temperature of the cell (°C)
T_∞	ambient temperature (°C)
T_{ISC}	internal short circuit temperature (°C)
T_{max}	maximum temperature during TR (°C)
T_{mr}	temperature at maximum rate (°C)
T_{react}	onset temperature for the self-heating reactions (°C)
T_{TR}	thermal runaway temperature (°C)
T_{max}	maximum cell surface temperature during the thermal runaway (°C)
T_{onset}	onset temperature (°C)
$(dT/dt)_{max}$	maximum self-heating rate (°C/min)
P	pressure (Pa)
P_d	dynamic pressure (Pa)
P_{ref}	ambient pressure (Pa)
u	VELOCITY of the airflow (m/s)
V	cell voltage (v)
W_i	density of the reactant
x	fractional degree of conversion

heater [13–18] and patch elements [19–21]. Some tests were also conducted with impinging fires [28–30].

ARC tests were often used to measure thermal properties like specific heat capacity and heat generation rates due to the decomposition reactions [27]. The average specific heat capacity of the battery allows conversion of the measured temperature rise into thermal energy. ARC can provide details on the critical degradation process at elevated temperatures during a thermally worst-case scenario in a closed adiabatic environment and self-sustaining TR conditions. In the tests, exothermic reactions were detected at a specific onset temperature, from which the cell component materials progressed to explosive decompositions and ultimately TR. Though, ARC tests are useful in analyzing LIB failure, they were not specifically designed for LIBs. It is not possible, for example, to quantify heat generation due to different decomposition reactions using ARC. In addition, ARC tests using the HWS protocol or under isothermal conditions generally take one to several days to reach TR.

Abuse tests through side heating can provide insight about TR propagation in clusters of cylindrical cells [12]. Many researchers investigated 18650 LIBs [23,29,31–35]. Golubkov et al. [23] evaluated 18650 LIBs with three different cathode materials in a pressure-tight reactor under external heating at a constant rate of ~2 °C/min. They recorded maximum cell surface temperature of 687 °C after ~5200 s. Chen et al. [29] used 2 kW coiled heater and measured heat release rate, mass loss, time to ejection and heat of combustion under different state of charges (SOC) from 25 to 100%. The time for the cell surface to reach its maximum temperatures of 524 to 756 °C varied from 380 to 325 s. Finegan et al. [31] studied cells at elevated temperatures (> 250 °C) by applying a heat gun to track the evolution of internal structural damage and thermal behavior during TR initiation and propagation. The cells were found to reach maximum temperatures between 168 and 217 s. Lammer et al. [32] conducted thermal ramp experiments in a furnace preheated to 80 °C and then at a thermal ramp rate of 0.5 °C/min. Maximum cell surface temperatures of 744, 631 and 496 °C were observed at 7902, 6300 and 4440 s for three 18650 cells with slightly different chemistry. Liu et al. [33] developed a novel Copper Slug Battery Calorimetry combined with oxygen consumption calorimetry to quantify the heat generation due to abuse reactions and flaming. They exposed 18650 cells with 25, 50 and 100% SOCs to a heating power of 20 W, maximum cell surface temperatures were measured as ~614 °C, 717 °C and 727 °C at ~2221 s, ~2019 s and ~1556 s, respectively. The heat generation due to flaming was found to be larger than the sum of the electric energy due to short circuit and abuse reactions.

Two recent publications of our team have addressed the TR characteristics of 21700 LIBs [10,20]. Chen et al. [10] tested 5 Ah 21700 cells of 30 and 100% SOCs subjected to uniform heating with a flexible heater of 20 W. The maximum cell surface temperatures were found to be 675–719 °C for 30% SOC and ~583–707 °C for 100% SOC in repeated tests. The corresponding times to reach the maximum temperature were ~1398–2875 s for 30% SOC and ~927–1066 s for 100% SOC. They also estimated the heat release rate (HRR) of the resulting fire from the flame height using established correlations for jet flames. More recently, further tests have also been conducted for the same cell with flexible and nichrome wire heaters of 20 W [20]. Maximum cell surface tempeature was recorded as 517 °C at 1219 s with the nicrome wire heater and 583.5–707.3°C at 937–1078 s with flexible patch heater. Elsewhere, Kang et al. [4] examined heat generation in the 21700 30T (1S18P) battery pack based on the power demand during train propulsion between two stations. Relefors [5] conducted ARC tests to determine the critical onset conditions of TR for three types of 4–5 Ah 21700 LIBs. For the NMC-based batteries, a distinct endothermic reaction was noted between 116 and 121 °C, an onset temperature of exothermic self-heating was estimated to be around 120 °C while an explosive decomposition was observed at about 170 °C. The maximum cell surface temperature observed was 590 °C after 42 h in HWS ARC tests.

Table 1 provides a summary of the abovementioned experimental investigations for cylindrical 18650 and 21700 LIBs. Most experiments used relatively low heating power of around 20 W or the HWS protocol with ARC. Due to the relatively low heating power, it typically took between 900 to over 2000 s for the cell to enter TR. For those tests involving patching heating elements [19–21], the readings were also likely affected by heat conduction through the cell canister which is generally made of good conductor. While some tests were performed with higher heating power for 18650 LIBs [31,36], no tests have been reported for 21700 LIBs subjected to localized heating on the surface with heating power larger than 20 W. It is, however, evident from Table 1 that LIB with the same SOC exhibits different TR characteristics under different heating conditions.

Table 1
Summary of the tests reported in the literature.

Ref.	Cell Type/ Dimensions	SOC	Heater type	Heating Power/ temperature (°C)	Time to reach maximum cell surface temperature (s)	Maximum cell surface temperature (°C)
Golubkov et al. [23]	18650	100	electric heater	-	-	687
Chen et al. [29]	18650	25	electric coiled heater	2 kW	380	524 ± 3
		50			360	667 ± 17
		75			353	736 ± 49
		100			325	756 ± 56
Finegan et al. [31]	18650	100	heat gun	>250 °C	168–217	-
Lammer et al. [32]	18650	100	electric furnace	Thermal ramp 0.5 °C/min	7902	744 ± 57
					6300	631 ± 85.5
					4440	496 ± 71.5
Liu et al. [33]	18650	25	copper slug battery	20 W	2221 + 27	614 ± 2
		50	calorimetry		2019 + 36	717 ± 5
		100			1556 + 46	727 ± 13
Kriston et al. [36]	18650	100	Coil heater	0.9–1.2 kW	-	741–830
Chen et al. [10]	21700	30	flexible patch heater	20 W	1398–2757	583–707
		100			927–1066	675–719
Chen et al. [20]	21700	100	ARC	HWS	1380–1446.2	710.7–762.1
			Flexible patch heater	~20 W	937–1078.4	583.5–707.3
			Nicrome wire	~20 W	1219	517
Relefors [5]	21700		ARC	HWS	-	589

The above review highlighted the lack of insight about the effect of localized thermal abuse for 21700 LIBs as well as heat generation by different abuse reactions during the evolution to TR. In addition, there is limited understanding about the effects of different heating methods on TR evolution and the critical temperature for TR onset. Kriston et al. [36] developed an alternative TR initiation method for LIBs using inductive heating and applied it to TR of 3.1 Ah 18650 LIB using relatively high power of 1–1.2 kW for 0.5–2 s. TR was triggered in all the cases and the cells lost structural integrity with opened casings. Their results indicated that only 1% of the cell's electric energy is sufficient to initiate TR. Higher heating powers have been used in tests for pouch cells, e.g. Jin et al. [37] tested 5.0 AH pouch LIBs with plate heater of 150 and 250 W. They observed maximum cell surface temperatures of 1000 °C after 1700 s for 150 W and at 700 s for 250 W heater power.

1.2. Knowledge gaps in modeling

Both two- and three-dimensional (2-D and 3-D) computational fluid dynamics (CFD) simulations have been conducted to study TR evolution induced by thermal abuse [21,38,39]. In such approach, the cell was considered as a solid block of 1-D, 2-D or 3-D with the abuse reactions addressed by different methods. The CFD framework simulates the interaction between the cell and the environment. A range of commercial software like COMSOL Multiphysics [4,34,36,39,41], ANSYS-CFX [40] and ANSYS-Fluent [41] have been used. The authors' group have modified the open source CFD code OpenFOAM to simulate the evolution from normal to abuse conditions and TR [42].

Kim et al. [41] extended the 1-D thermal abuse model of Hatchard et al. [43] to 3-D. This approach has also been adopted by others with some variations. Coman et al. [44] incorporated venting of the electrolyte and jelly roll (ejecta) into the thermal abuse model. They also developed 0-D and 3-D models to predict TR of 18650 LIB triggered by internal short circuit. The authors' group [20] proposed a simplified mathematical model for predicting heating induced TR of 21700 cells by using two Arrhenius expressions for the exothermic decomposition and autocatalytic reactions. The model was formulated as lumped 0-D, axisymmetric 2-D and full 3-D. The 0-D lumped model was recommended for predicting ARC tests when the Biot number is small, the 2-D axisymmetric model for axisymmetric heating conditions and the 3-D model for situations when neither of the above conditions can be met such as the flexible and nichrome wire heaters.

The abuse reactions during TR evolution can be considered with either detailed electrochemical models or simple thermal abuse models. In comparison, the complexity of the equations in the detailed electrochemical models places relatively higher demand on computing resource [45]. The simpler thermal abuse model has hence been adopted by many researchers (e.g. [43,44]) including the authors' team [20,42]. In such approaches, simplified kinetic parameters for heat addition were determined through ARC tests. Under adiabatic conditions in the calorimeter, the heat from the abuse reactions result in the increase of the cell surface temperature. Kinetic parameters for the exothermic reactions at different stages of the evolution to TR can be estimated based on the relationship between the measured rate of temperature rise and actual temperature rise in ARC tests [47–49]. Ping et al. [42] estimated the kinetic parameters for six different individual reactions. The input parameters required for each reaction were obtained by disassembling the cell to measure the thermal response of its components in differential scanning calorimetry (DSC). Chen et al. [20] proposed a simple two-stage reaction model, considering solid electrolyte interphase layer (SEI) and anode decomposition as the first stage and the heat generation by electrolyte and the cathode decomposition as the second stage. Such simplification does not distinguish the different stages of the abuse reactions and hence unable to quantify the associated heat generation. Others considred abuse reactions associated with the anode and cathode decompositions, electrochemical reactions and SEI decomposition separately (e.g. [24,50]). Thus, the kinetic parameters derived can also be used to estimate the associated heat generation rates.

In CFD analysis of LIBs, the kinetic parameters derived from the EV-ARC tests, the heat addition due to decomposition reactions are described by partial differential equations (PDE) and added to the energy equations for combined simulation of heat generation and dissipation. For the later, most previous simulations assumed constant heat dissipation with presumed heat transfer coefficients [12–15]. Such assumption neglected the fact that the actual convective heat transfer vary with tempearture evolution in the domain and the enviormental conditions. Furthermore, most previous simulations simply treated the cell with 0-D lumped model, neglecting the temperature gradient within the cell [20,46]. Such approach assumes isotropic thermal properties [34,35,51]. In practice, a relatively higher temperature gradient is expected in the cell. Improved accuracy can be achieved by considering anisotropic thermal properties [20,52], which requires 3-D cell model [20].

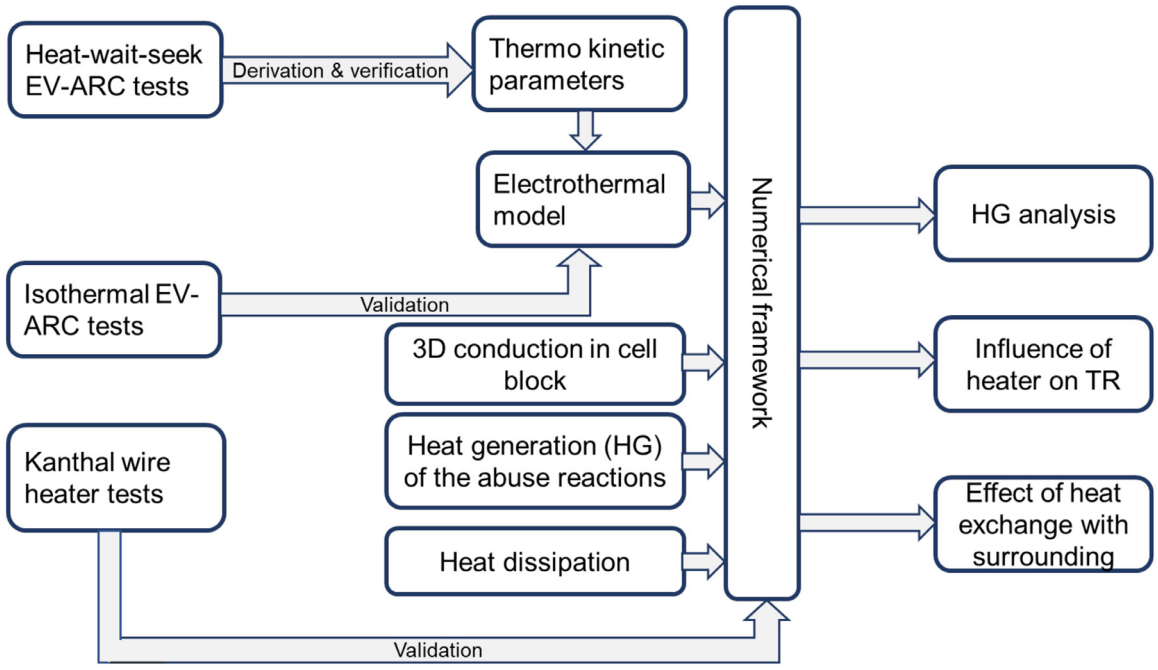

Fig. 1. The logic flow and structure of the manuscript.

In summary, previous simulations using a variety of commercial and opensource codes have laid the foundation for the modeling framework to combine thermal abuse models and cell behavior with surrounding air domain. However, all previous attempts in such context treated the cell with 0-D lumped model with isotropic thermal properties, neglecting the temperature gradient within the cell. Such treatment is inherently problematic as a relatively higher temperature gradient is expected in the cell.

In the present study, combined experimental and numerical studies have been conducted for 4.8 Ah 21700 LIBs at 100% SOC, which is the worst-case scenario in the context of safety. The experiments involved both HWS and isothermal EV-ARC as well as Kanthal wire heaters. The kinetic parameters were derived from one of the HWS tests and implemented in OpenFOAM. The jelly roll stack of the cell is assumed to be a 3-D block with anisotropic thermal conductivities. The predictions were firstly verified by the remaining two HWS tests not used in the derivation of the kinetic parameters; and then validated with the temperature measurements of the isothermal EV-ARC tests. The validated model was subsequently used to predict the TR onset temperature in simulated EV-ARC environments. Finally, the model was further validated with the Kanthal wire tests. The 3-D predictions have also been used to provide insight about the heat generation rate, time to maximum TR temperature and the influence of heating power/arrangement as well as the effects of heat dissipation. Fig. 1 illustrates the logic flow and structure of the manuscript.

The key *innovation* of the manuscript includes:

- Pioneering CFD predictions incorporating 3-D conduction in the cell with anisotropic thermal conductivities, HRRs of the abuse reactions and the surrounding air domain.
- Pioneering CFD predictions of TR onset temperature in simulated isothermal ARC environments.
- Novel experimental techniques to address localized thermal abuse for 21700 LIBs under large heating powers up to 5 times that used in the published tests.
- Innovate use of the CFD predictions to provide insight about parameters which are difficult to quantify experimentally, including HRRs of different abuse reactions and the effects of heat dissipation.
- Novel use of the validated CFD model to conduct numerical experiments examining influence of different heating and cooling arrangements.
- The sensitivity of the time to thermal runaway under different heating methods and convective cooling were analyzed to formulate safety recommendations.

2. Heat generation during TR evolution and heat-wait-seek EV-ARC tests

The EV-ARC, which has an extended volume for large format LIBs, was used to test 21700 LIBs with $Li(Ni_xMn_yCo_z)O_2$ cathodes and graphite/silicon anode (NMC). The capacity and nominal voltage of the cell are 4.8 Ah and 3.7 V, respectively. The cells were fully charged to 100% SOC before the tests. The cell surface temperatures were monitored to obtain the self-heating rate of the cell. Thermal Hazard Technologies, the manufacturer of the EV-ARC has stated in their products information sheet that its heating rate is in the order of 10 K/s. Three tests were conducted using the HWS protocol. The thermo kinetic parameters of the Arrhenius equations for the volumetric heat generated from the abuse thermal reactions were determined using the measurements from one of the three tests while the measurements of the remaining two tests were used for model verification to be described in Section 4.

2.1. Heat generation during TR evolution

The abuse reactions due to decomposition of cell materials occur in various temperature ranges, releasing heat and gas [54]. The volumetric heat generated from the abuse thermal reactions can be evaluated by (e.g. [55,56]):

$$\dot{Q}_{exo} = \dot{Q}_{SEI} + \dot{Q}_{An} + \dot{Q}_{Ca} + \dot{Q}_{Mix} \quad (1)$$

where, $\dot{Q}_{SEI}$ is the heat due to decomposition of SEI layer, $\dot{Q}_{An}$ is the heat due to decomposition of anode, $\dot{Q}_{Ca}$ is the heat due to de-

composition of cathode and $\dot{Q}_{Mix}$ is the heat due to decomposition of electrolyte and other remaining materials including the binder as well as heat generated by the earlier combustion following ejection. This will be explained in more detail in Section 3.2.

It is assumed that $\dot{Q}_i$ (i=SEI, An, Ca, and Mix) is related to the rate constant of the reaction κ_i, which follows an Arrhenius equation, and can be expressed as follows (e.g. [43,57]):

$\dot{Q}_i = W_i H_i \kappa_i$, and

$$\kappa_i = A_i \exp\left(-\frac{E_i}{k_b T}\right) c_i \text{ and } \frac{dc_i}{dt} = -\kappa_i \quad (2)$$

where, W_i denotes the density of the reactant, H_i the reaction heat, c_i the normalized amount of the reactant, A_i the pre-exponential factor for the reaction, E_i the activation energy for the reaction, and k_b is the Boltzmann's constant. The $W_i H_i$ was calculated based on the change in temperature at different reaction stages expressed as $W_i H_i = \Delta H_i / V_{cell}$. Here, V_{cell} is the volume of the cell. The cell was treated as a 3-D block with anisotropic thermal conductivities following our previous study [20], which suggested the need for 3-D as neither lumped 0-D nor axisymmetric heating conditions were applicable here. The heat generations from the four different reactions were divided equally into each control volume within the cell block and feed to the temperature calculations for each time step. The average temperature of all the control volumes in the cell block was then used to calculate the heat calculations with Eq. (2) for the next time step.

2.2. The reaction kinetics

During the self-heating stage, the cell temperature increases exponentially as heat generation by the exothermic abuse reactions are far greater than heat dissipation through the battery thermal management system. The LIB temperature rise in an adiabatic environment can be determined following previous work (e.g. [21,58]) and described by Eq. (3):

$$\frac{dT}{dt} = \Delta T_{ad} . A_i \cdot \exp\left(\frac{-E_i}{k_b T}\right) . (1-x)^n \quad (3)$$

where, x is the fractional degree of conversion with an initial value of 0, A_i the pre-exponential factor for the reaction and n is reaction order, respectively. By taking natural logarithm on both sides:

$$ln\frac{dT}{dt} = \ln(\Delta T_{ad} . A_i) - \left(\frac{E_i}{k_b T}\right) + ln(1-x)^n \quad (4)$$

If the frequency factor is greater than that of $(1\text{-}x)^n$, Eq. (4) can be simplified to:

$$ln\frac{dT}{dt} \approx \ln(\Delta T_{ad} . A_i) - \left(\frac{E_i}{k_b T}\right) \quad (5)$$

where, E_i and A_i can be obtained from the slope and intercept of the fitting curve of $ln(dT/dt)$ versus $1/T$ plots.

2.3. Heat-wait-seek tests

A schematic diagram of the experimental set up is illustrated in Fig. 2. An open throne was used to hold the cell in an upright position and prevent it from being fired across the EV-ARC chamber of 4.3 L volume during the test. The cell is insulated to reduce heat transfer to and from the metal throne as shown in Fig. 2. The thermocouples were located on the side and middle height of the cell. Several additional thermocouples were placed inside the canister atmosphere and at the top and bottom of the cell.

The tests were performed by Thermal Hazards Technology. Fig. 3(a) shows the measured profiles of the voltage, cell surface temperature and temperature rate response. Fig. 3(b) details the main exothermic reactions inside the cell during different stages. The LIB temperature increased with the heating from the EV-ARC. The self-heating reactions, i.e. decomposition of SEI layer, anode and cathode material and the electrolyte were not initiated during the initial stage. The onset temperature for the self-heating reactions (T_{react}) started after the cell surface temperature reached 93.08 °C. The voltage of the battery decreases with the increase of its temperature. The SEI film starts to decompose at 93.08 °C, resulting in the reaction between the electrolyte and graphite anode. Both reactions contribute to a slow rise in the temperature of the cell. The voltage dropped from 4.06 to 1.8 V at 102 °C, indicating micro short circuit inside the cell, which induced further heat accumulation inside the cell and led to further temperature increase. As the temperature built up further, the separator collapsed, leading to further large-scale short circuit inside the cell as shown in Fig. 3(a) between 126 and 195 °C. Subsequently, the cathode and anode materials, electrolyte and other materials inside the cell decomposed drastically and the temperature started to rise exponentially.

The maximum self-heating rate $(dT/dt)_{max}$, internal short circuit temperature (T_{ISC}), maximum temperature during TR (T_{max}) and heat released during TR (ΔH) can be derived from the measurements in Fig. 3(a) and (b). The start temperature was set to 40 °C. Heating was increased gradually at a temperature step of 5 °C. The maximum test temperature was 420 °C. When the cell surface exceeds this temperature, the calorimeter stopped heating. The waiting time was set to 60 min for each temperature increase. After reaching thermal equilibrium during the waiting period, the system entered the seek period of 10 min. During this period, the self-heating rate of the cell was monitored by tracking the temperature rise. The point at which the self-heating rate detected a larger value than the exothermic sensitivity, which was set to 0.02 °C/min, was treated as the onset of exothermic reactions. The heating of the EV-ARC was paused, the corresponding temperature rise due to internal exothermic reactions was recorded till the end of TR. If a temperature change rate smaller than the exothermic sensitivity was detected again, the system would switch back to the heating mode.

Fig. 4(a) shows the measured transient temperature profiles on the top, side and bottom zones in the EV-ARC chamber with the maximum being ~180 °C. As the calorimeter heats much more slowly than the cell, at the time the cell reached its maximum temperature of ~750 °C, the calorimeter temperature was only ~180 °C. Fig. 4(b) illustrates the HWS testing protocol. Table 2 summarize the specifications of the HWS tests.

2.4. Evaluation of the thermo kinetic parameters

Although as shown earlier in Fig. 4, the temperatures measured inside the EV-ARC calorimeter were below 180 °C, the measured cell surface temperatures went well above this during TR due to self-heating. Fig. 5(a) shows the rate of temperature rise *vs* cell surface temperature. From 132.45 °C onwards, the temperature rise accelerates sharply till the maximum cell surface temperature. This was hence treated as the onset temperature T_{onset} of the self-heating stage. Plotting $ln(dT/dt)$ versus $1/T$ in Fig. 5(b), the E_i and A_i can be obtained from the slope and intercept of the fitting curve for Eq. (5). The associated heat release can be calculated by:

$$\Delta H = m_{battery} . C_p . (T_{max} - T_{TR}) \quad (6)$$

where, $m_{battery}$ is the mass of the test cell; Cp is the total heat capacity for the sample LIB, which is around 900 (J/kg•K) that measured by the EV-ARC, T_{TR} and T_{max} are thermal runaway and the maximum cell surface temperature during the thermal runaway (K), respectively.

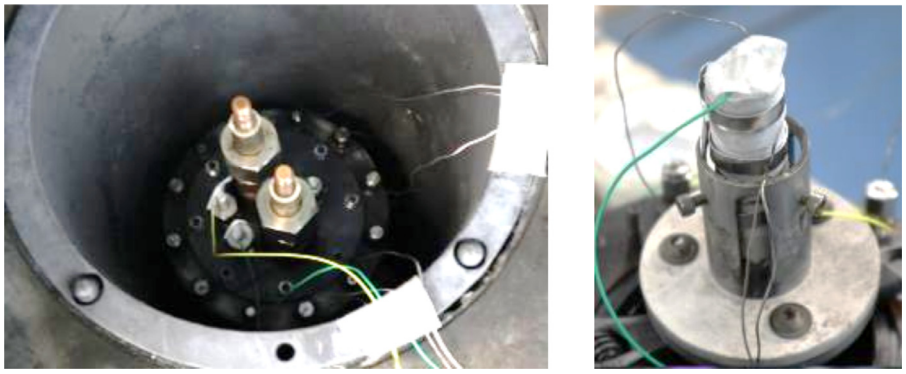

Fig. 2. The EV-ARC chamber (left) and Cell placed in a metallic throne (right).

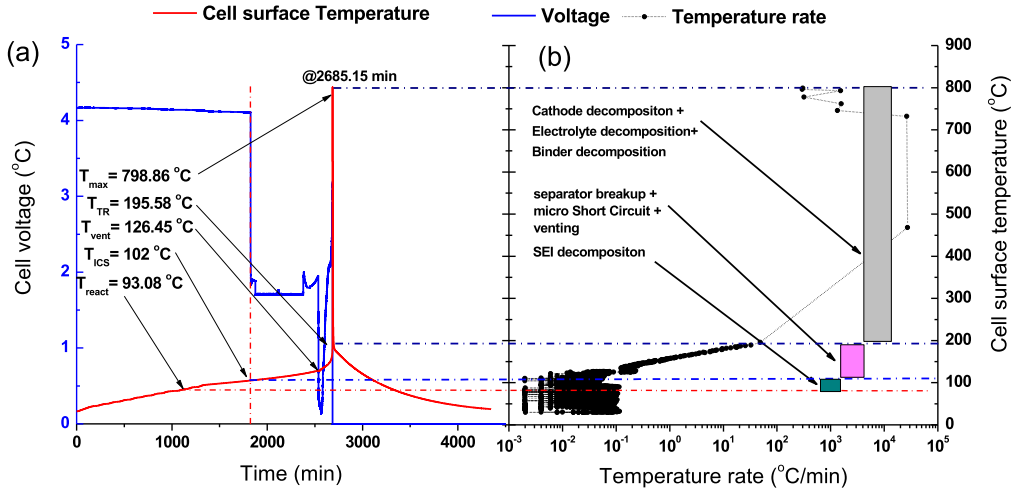

Fig. 3. Cell surface temperature, temperature rate responses and exothermic chemical reactions inside the LIB in Test 1.

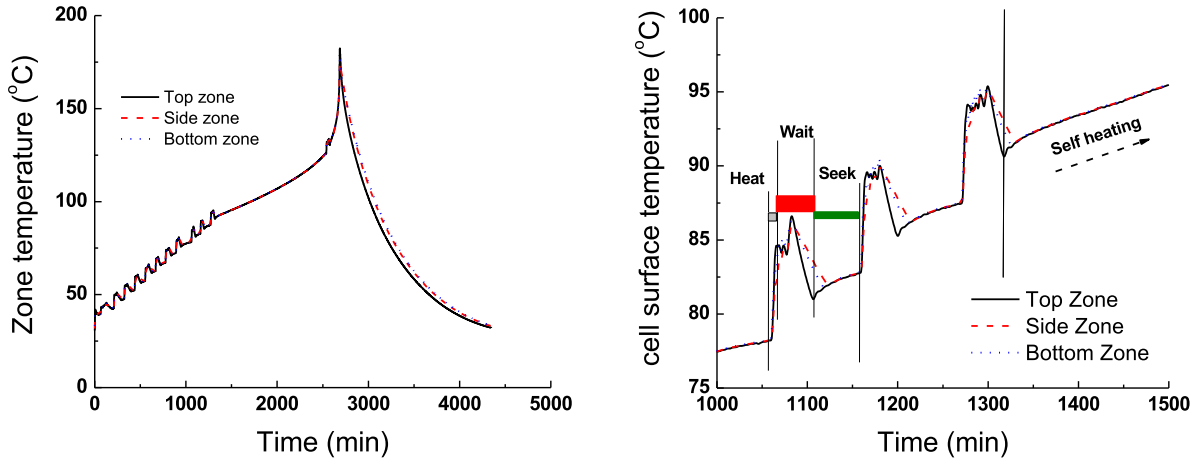

Fig. 4. The measured transient temperatures inside the EV-ARC calorimeter (a) at the side, top and bottom zones in Test 1; (b) Heat-wait-seek protocol.

It should be noted that there are some overlapping of the exothermic reactions in some temperature ranges. The exact temperature ranges for the decomposition of SEI layer, anode, cathode and the electrolyte and other remaining materials including binder are dependent on battery specifications [50]. DSC tests [42,60] are needed to determine kinetics parameters of each separate exothermic reaction. Due to limited information about the chemical compositions of the 21700 cell, the activation energy and the reaction exponents, at the first three reaction stages (decomposition of SEI, anode and cathode) were taken from Refs. [41,43] based on the similarities of the cell materials. In these stages, the decomposition of the electrolyte and other materials was neglected as even if their decomposition already started, the heat generation rates were very small in comparison with that due to SEI, anode and cathode. The effect of change in the thickness of the SEI layer was not considered [43]. As noted by previous researchers [29], the relatively large amount of heat generated during the last stage was partially due to the ignition of released combustible gases and/or

Table 2
Specifications of the HWS EV-ARC tests.

		Test 1	Test 2	Test 3
Reaction onset temperature (°C)	T_{react}	93.08	98.34	93.42
Self-heat rate at t_0 (°C/min)	dT/dt	0.023	0.028	0.022
Temperature at maximum rate (°C)	T_{mr}	467.96	637.89	555.53
Maximum self-heat rate (°C/min)	$(dT/dt)_{max}$	27191	10734	17937
Final adiabatic temperature (°C)	T_{ab}	798.86	741.42	755.1
Adiabatic temperature rise (°C)	δT_{ab}	705.78	643.08	661.68
Heat of reaction (J/g) $\delta H = C_p \cdot \delta T_{ab}$	δH	635.2	578.77	595.51
Cell mass (g)	$M_{battery}$	68.40	68.16	68.24
Total heat of reaction (kJ) $\Delta H = \delta H \cdot m_{battery}$	ΔH	43.45	39.45	40.64
Exotherm time (min)	t_{ex}	1312	1012.6	1309.6

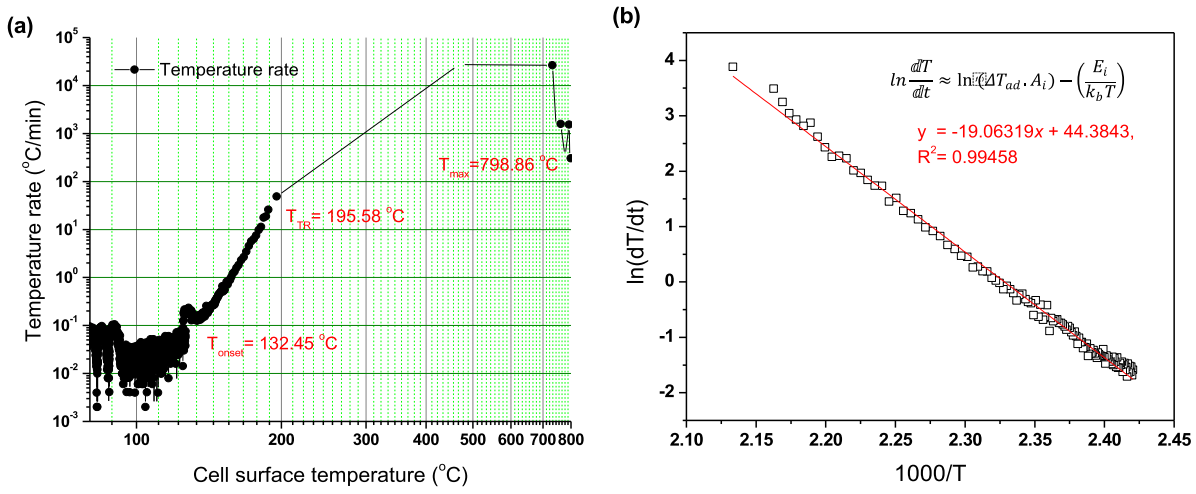

Fig. 5. Self heating stages (a) Temperature rising rate *vs* cell surface temperature (b) Plot of ln(dT/dt) *vs* 1000/T; the solid line was used to estimate the values of E_a and A.

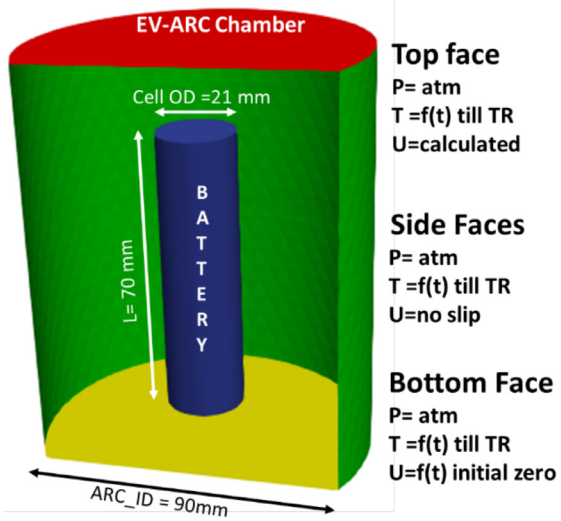

Fig. 6. The computational domain and boundary conditions.

flammable electrolyte. For simplicity, the combined heat generation due to the decomposition reactions of electrolyte and other remaining materials including binder and any remains of the anode and cathode as well as some due to combustion of the released flammable gases was considered together as $\dot{Q}_{Mix}$ as shown in Eq. (1). As shown in Fig. 5, the maximum cell surface temperature were well above the auto-ignition temperature of the released flammable gases which range from 450 °C for some hydrocarbons, 580 °C for hydrogen and 609 °C for carbon monoxide. It was likely that $\dot{Q}_{Mix}$ may include the contribution from combustion after the ignition of the released flammable gases. The thermo kinetics parameters were estimated by fitting the test data of the temperature versus time in Test-1. The normalized amount of all the reactants (c_i mentioned in Eq. (2)) was assumed to be 1 at the initial step and subsequently their rates of change follow Eq. (2).

The heat generation in the first three stages were mainly due to the decompositions of the SEI layer, anode, and cathode. The heat produced by these three exothermic reactions under adiabatic condition was calculated per unit volume of 21700 cells based on the available data for 18650 NMC cells in [59] due to similarities of the cell materials. Although such adoption may introduce some errors due to possible small differences in the electrodes between the two types of cells, the influence should be trivial. The combined heat generation due to the decomposition reactions of electrolyte and other remaining materials including the binder as well as the earlier combustion which started during this stage was calculated using Eq. (6) as $\dot{Q}_{Mix}$. The thermo reaction kinetics and related parameters for all four stages of the abuse reactions are listed in Table 3.

3. Numerical framework

The cell was simulated as a solid region. Its heat exchange with the environment was considered by convective cooling through an air domain surrounding the cell. The heat generation within the cell due to irreversible chemical reactions is calculated using the Arrhenius equations derived from the current EV-ARC tests following Coman et al. [21].

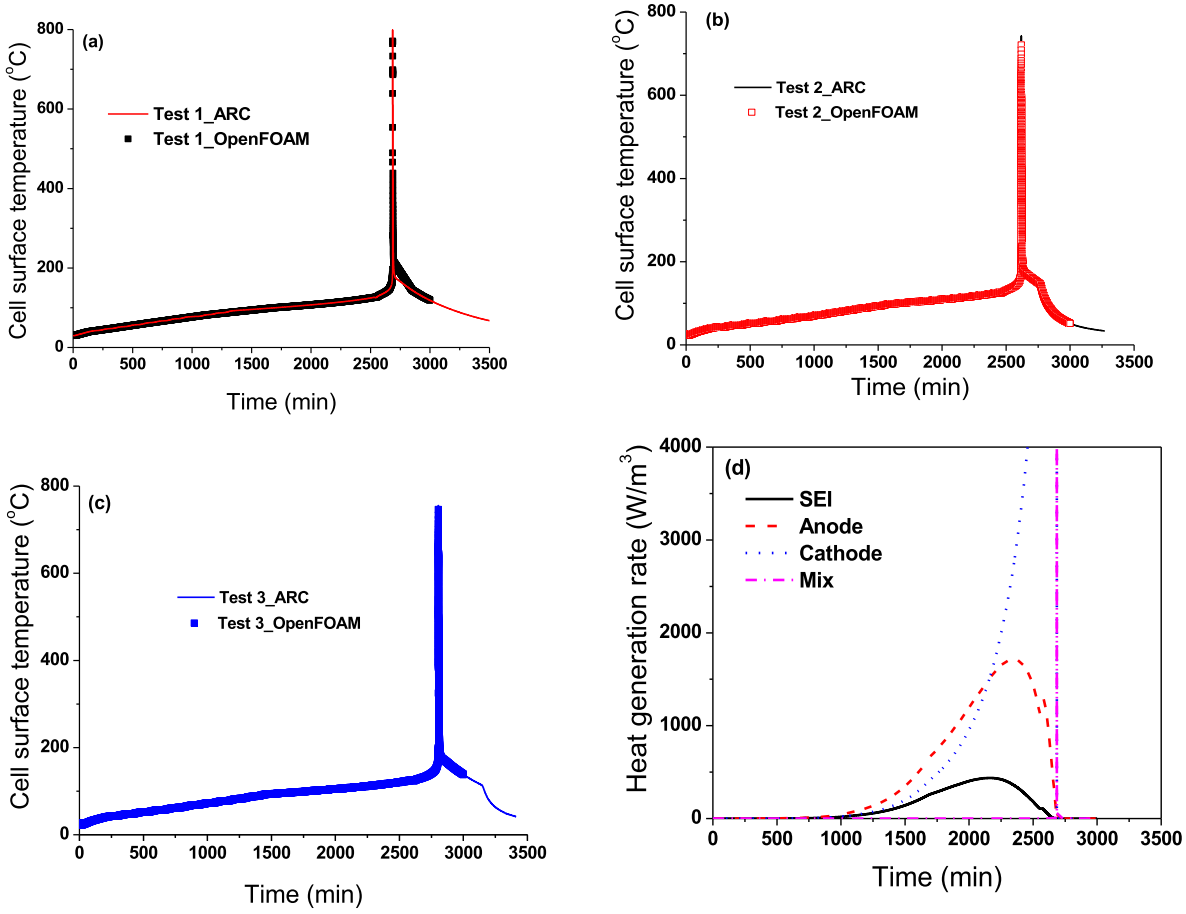

Fig. 7. Comparison between the predicted and measured cell surface temperatures (a) Test, (b) Test 2, (c) Test 3 (d) Evolution of heat generation rate during Test 1.

Table 3
Parameters used in the thermal abuse model.

Dominant exothermic reactions	W_iH_i (J/m^3)	A_i (s^{-1})	E_i (J/mol)	$c_{i,0}$
Decomposition of SEI	6.5763e7**	1.14e14 [43]	1.35e5 [43]	1.00
Anode decomposition	7.3410e7**	7.18e13 [43]	1.35e5 [43]	1.00
Cathode decomposition	2.06e9**	6.67e13 [41]	1.40e5 [41]	1.00
Q_{mix}	1.79e9*	5.12e15*	1.70e5*	1.00

* calculated from Eq. (5). **calculated based on the available data for 18650 NMC cell in [59].

3.1. Energy balance equation

The cell was represented by a solid structure formed with homogeneous layers. Some of the chemical and electrical energy stored in the cell was assumed to convert into thermal energy during the evolution to TR [50]. The exact amount of the electrical energy converts to heat is related to the LIB type and abuse conditions. Thermal conduction was assumed to be dominant in the solid cell zone. A cylindrical battery cell typically has a "jelly-roll-like" layered structure, which is homogenized and assumed to be one block with anisotropic thermal conductivities while the other properties are uniform. As OpenFOAM uses Cartesian coordinates, conversion to local cylindrical coordinates is needed for the anisotropic thermal conductivities of the jelly roll inside the cylindrical cell. The energy balance equation in cylindrical coordinates can be written as [53]:

$$\rho C_p \frac{\partial T}{\partial t} = \frac{1}{r}\frac{\partial}{\partial r}\left(\lambda r \frac{\partial T}{\partial r}\right) + \frac{1}{r^2}\frac{\partial}{\partial \phi}\left(\lambda \frac{\partial T}{\partial \phi}\right) + \frac{\partial}{\partial z}\left(\lambda \frac{\partial T}{\partial z}\right) + Q_{exo} - Q_{conv} - Q_{rad} \quad (7)$$

where, ρ is the density, kg/m^3; Cp is the specific heat capacity of the cell (J/kgK); λ is the thermal conductivity (W/mK). Q_{exo} is heat due to the irreversible reaction of TR (W), Q_{conv} is the heat source of the convection (W), Q_{rad} is the heat source of the radiation (W).

For the surrounding air domain, the following equations were employed:

Continuity:

$$\frac{\partial \rho}{\partial t} + \nabla.(\rho u) = 0 \quad (8)$$

Momentum:

$$\frac{\partial (\rho u)}{\partial t} + \nabla.(\rho u.u) = \nabla.(u \nabla u) - \nabla P_d - \nabla \rho g H \quad (9)$$

Energy:

$$\frac{\partial (\rho H)}{\partial t} + \nabla.(\rho u) - \nabla.(k \nabla H) = \frac{\partial P}{\partial t} + u.\nabla P \quad (10)$$

The total pressure p is determined by:

$$P = P_d + \rho g H + P_{ref} \quad (11)$$

where u is the velocity of the airflow; μ is the effective viscosity; P is the pressure; P_d and P_{ref} are the dynamic pressure and ambient pressure; g is the gravitational acceleration.

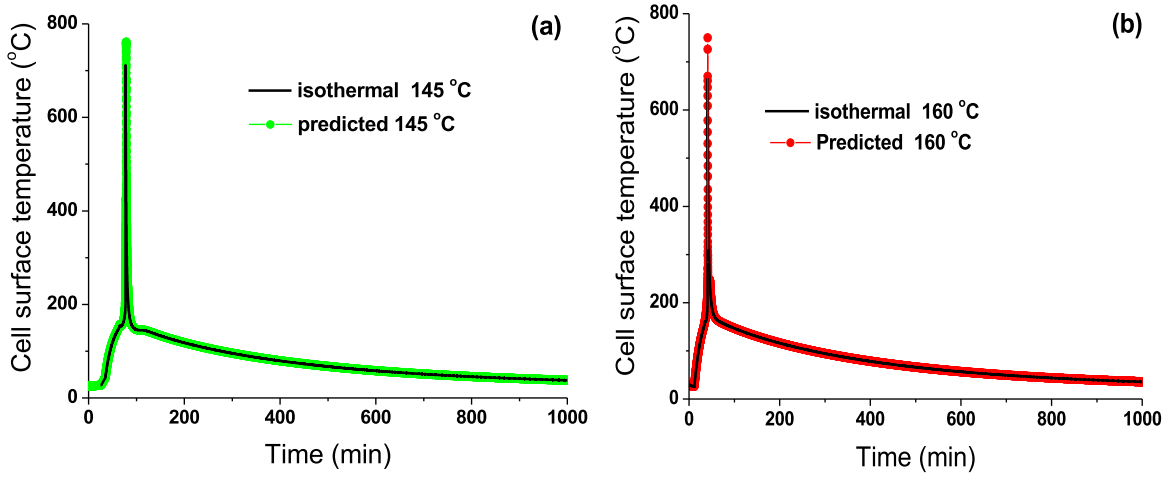

Fig. 8. Comparison of the predicted and measured cell surface temperatures.

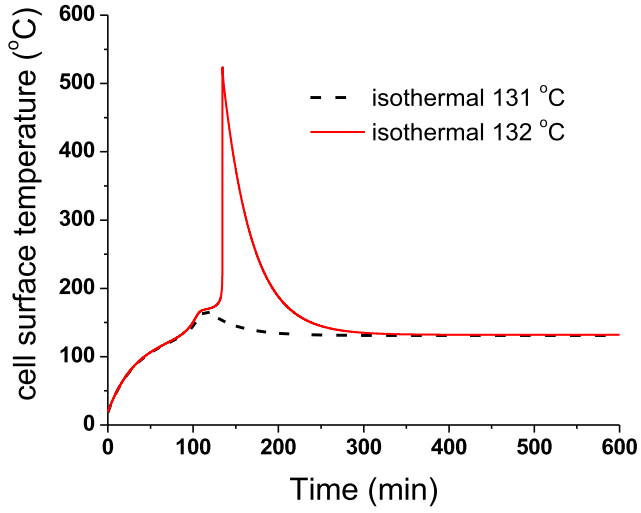

Fig. 9. Comparison between the predicted cell surface temperatures for simulated isothermal heating in EV-ARC environment under 131 and 132 °C.

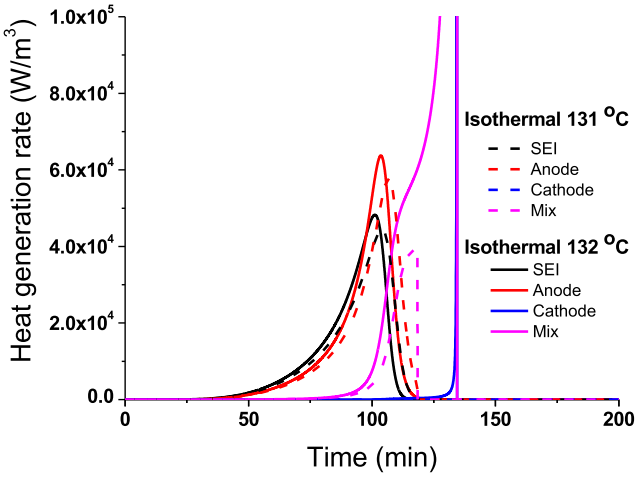

Fig. 10. Comparison between the predicted heat generation rates in the simulated isothermal heating in EV-ARC environment under 131 and 132 °C.

3.2. Heat dissipation

The heat exchange between the solid cell and air environment is calculated using the boundary patch available in OpenFOAM. Convective heat flux to the cell surface is evaluated following the Newton's law of cooling:

$$Q_{con} = h.A_{cell}(T_{cell} - T_{\infty}) \quad (12)$$

where, h_{conv} is convective heat transfer coefficient (W/m^{2}K), A_{cell} is the surface area of the cell (m^2), T_{cell} is the surface temperature of the cell (K), T_{∞} is the ambient temperature (K). The radiative heat flux out to the boundary is evaluated in the following equations:

$$Q_{rad} = \varepsilon.\sigma.A_{cell}\left(T_{cell}^4 - T_{\infty}^4\right) \quad (13)$$

where, ε is the average effective emissivity and σ is the Stefan–Boltzmann constant.

3.3. The modeling approach and solution procedure

Finite volume discretization and variable time step are employed. The heat generation due to four different irreversible chemical reactions represented by Eqs. (1) and (2) was divided equally into the computational volume of the cell and added as source terms in the energy equation. Anisotropic thermal conductivity was used to solve the heat transfer equation in the local cylindrical coordinates for the jelly roll. The cell was treated as a 3-D block with anisotropic thermal conductivities. The spatially averaged predicted temperatures of all the discretized finite volumes in the solid-cell region was calculated at every time step and used to evaluate the volumetric heat generation rate by the decomposition reactions in further loop and added to each finite volume. This approach is computationally more efficient than solving the decomposition reactions using the temperature value of each control volume.

Heat transfer with the surrounding air is solved through the continuity, momentum and energy equations to incorporate heat transfer with the surroundings. The surface temperature is calculated at the middle on the side of the cylindrical cell surface. The rapid temperature change during TR was captured using adaptive time steps.

4. Model verification with measurements from the remaining two HWS EV-ARC tests

To verify the derived thermo kinetic parameters derived from the first HWS test, numerical simulations were conducted for the remaining two HWS EV-ARC tests. The schematic of the computational model is illustrated in Fig. 6. The cell was represented by

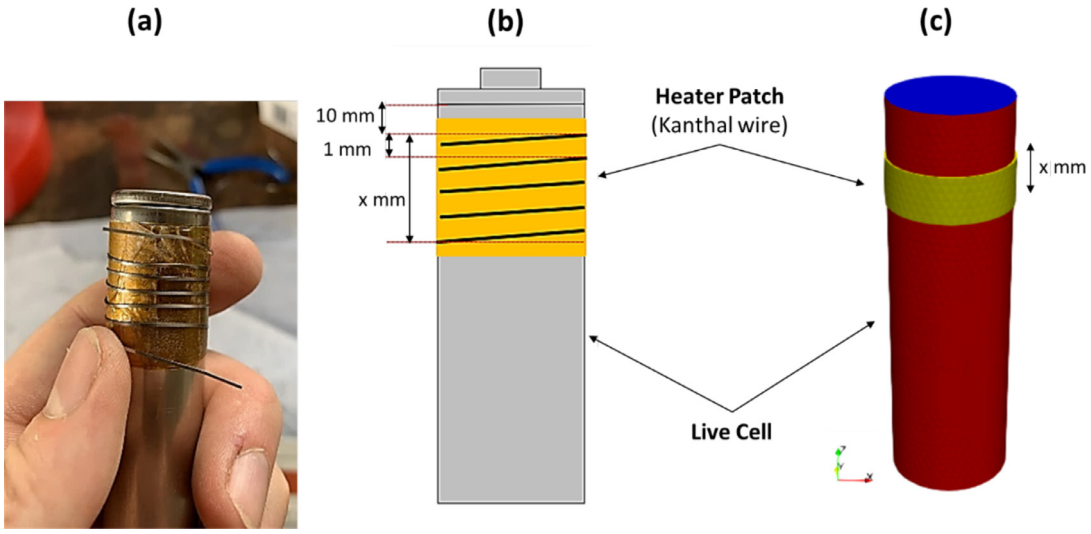

Fig. 11. The experimental and computational set-up for the tests with Kanthal wire heaters (a) A cell with the Kanthal wire heater (b) 2D sketch of the cell computational model, (c) Cell with the Kanthal wire heater in the computational domain.

Table 4
Summary of the predictions and measurements in the HWS tests.

Test Parameters	Test 1	Test 2	Test 3
Measured time to the maximum surface temperature (min)	2685.15	2618.38	2804.29
Predicted time to the maximum surface temperature (min)	2685.83	2618.95	2804.53
Relative difference between the above (%)	0.025	0.022	0.0086
Measured maximum cell surface temperature (°C)	798.85	741.42	755.10
Predicted maximum cell surface temperature (°C)	764.32	720.93	746.49
Relative difference between the above (%)	-4.32	-2.76	-1.14

a cylindrical solid region (21700 LIB cell) with 0.0105 m diameter and 0.070 m height. The surrounding air in the EV-ARC cylindrical chamber was enclosed in a computational domain of 0.045 m in radius and 0.1 m in height with time dependent temperatures.

The temperature profiles presented in Fig. 4(a), for the inner surface of top, side and bottom zones of the calorimeter were used as the boundary conditions, which were applied till the self-heating detected by the EV-ARC tests as shown in Fig. 4(b). Subsequently, the cell went into TR due to irreversible heat addition. The interfaces between the solid region of the cell and surrounding air were explicitly coupled and mapped for the boundary conditions.

Fig. 7(a–c) show comparison between the predicted and measured temperatures in all the three tests. The two additional tests were conducted to check the repeatability of the tests and verify the effectiveness of estimated kinetics parameters and the proposed model. Fig. 7(d) depicts the evolution of heat generation rate due to the abuse exothermic reactions including the decompositions of SEI, anode, cathode electrolyte and other remaining material denoted as $\dot{Q}_{Mix}$. All four reactions follow the same pattern, but $\dot{Q}_{Mix}$ increased sharply at the time of the maximum cell surface temperature, indicating the start of combustion as discussed earlier.

Table 4 provides a summary of the CFD predictions and measurements in the HWS EV-ARC tests. The predicted and measured times to thermal runaway occurrence are in excellent agreement with the largest discrepancy being less than 0.025%. Relatively larger discrepancies are found between the predicted and measured maximum cell surface temperatures, but the largest discrepancy is 4.3%. This might be partly due to the loosing of the contact between the thermocouples and the cell surface after TR. Overall, the good agreement indicates that the derived kinetics parameters and modeling approach can capture well the evolution to TR in EV-ARC environment.

5. Validation with isothermal EV-ARC tests and predictions of TR onset temperature

5.1. Validation with isothermal EV-ARC tests

To further validate model with the kinetic parameters derived from the HWS EV-ARC test for other thermal abuse conditions, isothermal EV-ARC tests were conducted using the same facility. The computational domain was kept the same as that of the HWS tests. The wall temperature of the EV-ARC chamber was kept constant (isothermal) at 130, 145 and 160 °C to mimic the isothermal tests till the cells went into TR. The hard casing outside the jelly roll is made of thin aluminum with isotropic thermal conductivity. As mentioned in Section 3.3, by using the spatially averaged temperatures of all the discretized finite volumes in the solid-cell region to evaluate the volumetric heat generation rate by the exothermic abuse reactions resulted in a significant reduction in the computational time in comparison with solving the decomposition reactions using the temperature value of each discretized finite volume and adding the heat into the energy equation.

Two repeated tests were carried out at 130 °C. Each time, the cell was left in the environment for more than a day, but TR was not triggered as heat production was balanced by the heat dissipation. Fig. 8 shows the comparison between the predicted and measured cell surface temperatures in the middle height for both cases are in very good agreement.

Table 5 compares the predicted and measured temperature evolutions for isothermal abuse conditions with the largest discrepancy being less than 0.68%. Relatively larger discrepancies of 6.75% are found between the predicted and measured maximum cell surface temperatures. This agreement indicates that the proposed model with the derived kinetics parameters can also capture the

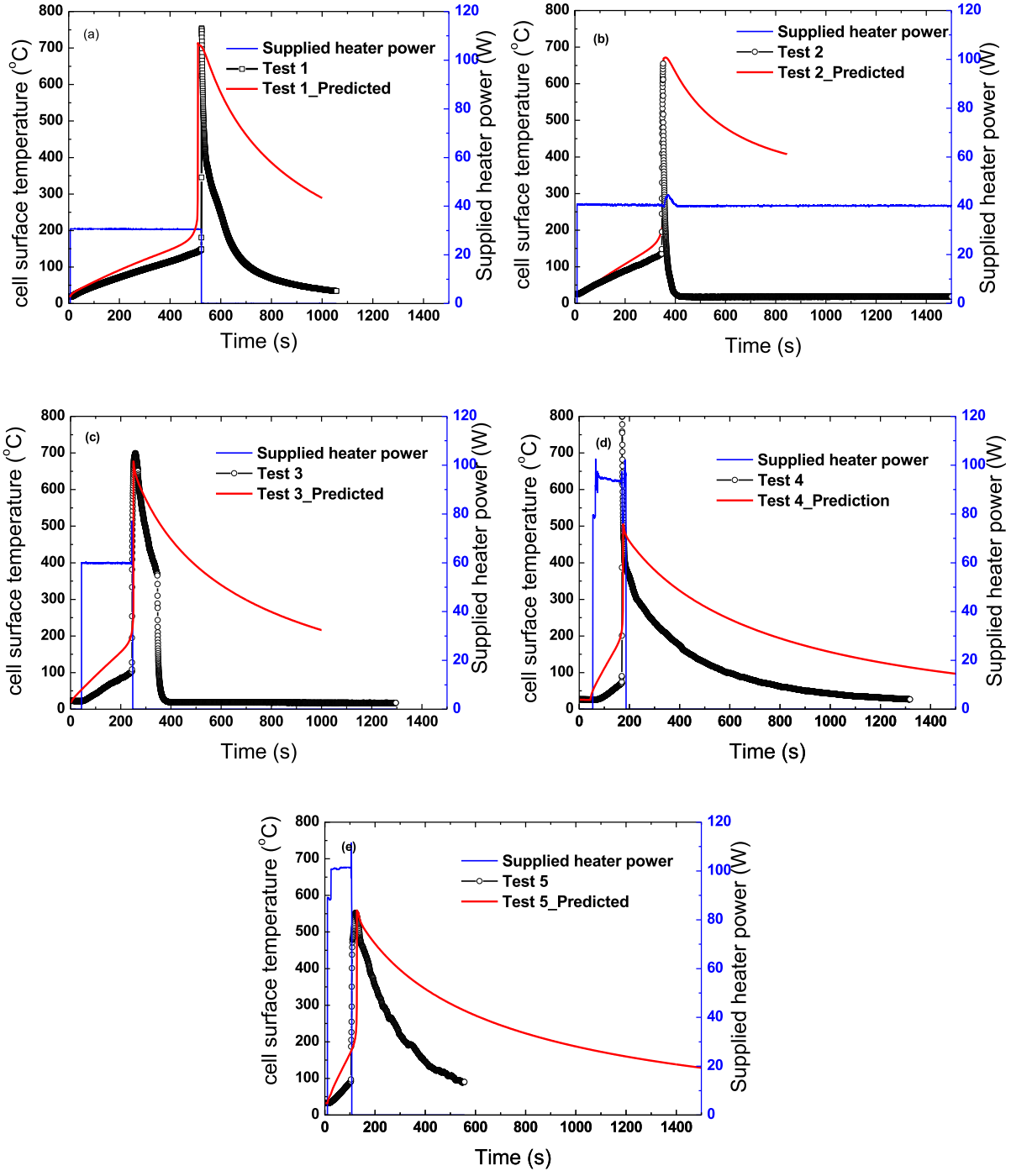

Fig. 12. Comparison between the predicted and measured cell surface temperatures for the tests with Kanthal wire heaters.

Table 5
Summary of the predictions and measurements in the isothermal EV-ARC tests.

Test	Max cell surface temperature (°C)		Relative error (%)	Time to max cell surface temperature (min)		Relative error (%)
	Measured	Predicted		Measured	Predicted	
Isothermal 132 °C	–	540.01	–	–	140.05	–
Isothermal 145 °C	737.05	749.68	1.71	41.16	41.07	0.21
Isothermal 160 °C	711.06	759.04	6.75	77.27	77.8	-0.68

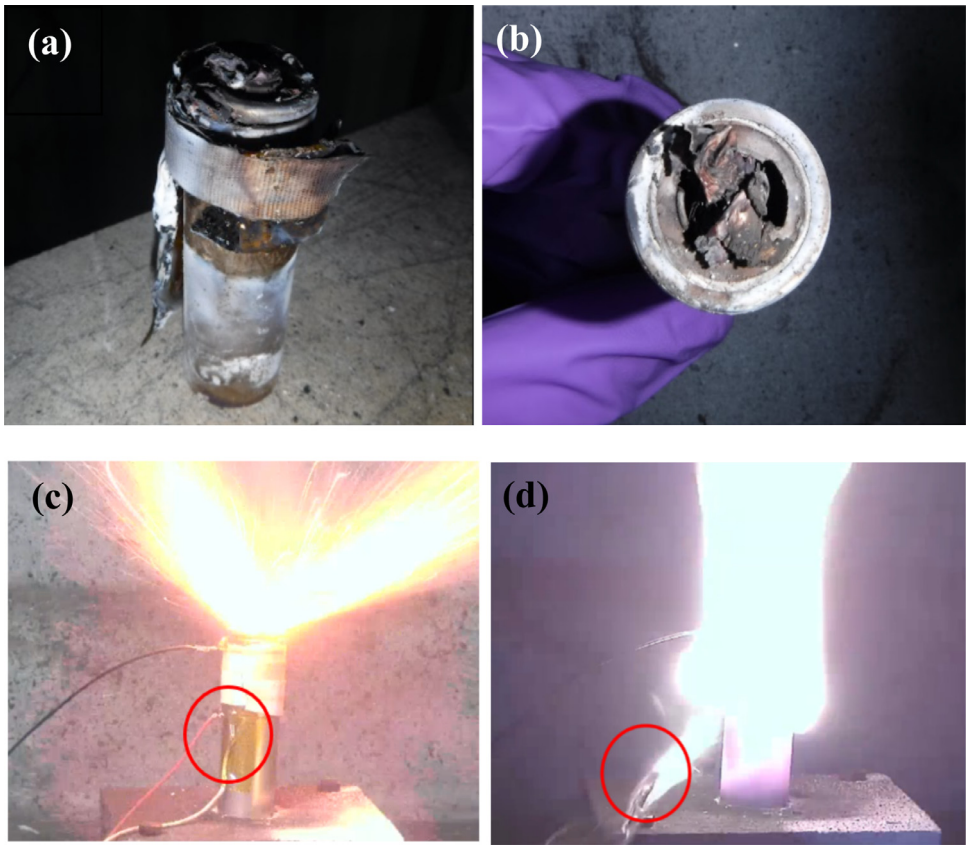

Fig. 13. Cell sample collected after tests (a) rupturing of cell in Test 3, (b) ejection of a part of jelly roll from the top of the cell in Test 4 (c) Position of thermocouple during TR in Test 2, (d) position of thermocouple after TR in test 2 (loosing of contact).

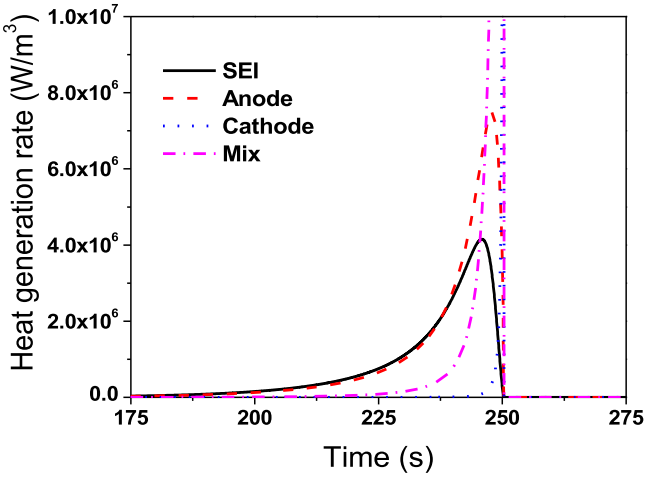

Fig. 14. The predicted heat generation rate for Test 3.

thermal behavior under the isothermal heating condition for the same cell.

In the HWS tests as reported in the previous section, the self-heating reactions were found to start after the cell surface temperature reached 93.08 °C. These results further highlight the difference between the HWS protocol and isothermal heating. In the former, the cell was exposed to continuous heating while in the later it is exposed to a constant temperature environment. It took more than 44 h for the cell surface to reach its maximum temperature in the HWS tests. As Table 5 shows the time to maximum cell surface temperature was 77.27 and 41.16 min for the 145 °C and 160 °C tests, respectively.

5.2. Predictions of TR onset temperature

To determine the TR onset temperature or the critical temperature to trigger TR, numerical simulations were carried out to mimic the isothermal tests in EV-ARC with temperatures from 100 to 145 °C. As shown in Fig. 9, the cell was found to enter TR when the temperature was equal or greater than 132 °C. Isothermal abuse at 131 °C or lower temperatures failed to trigger TR. The onset temperature to trigger TR of the considered 21700 cell is hence considered to be between 131 and 132 °C. As shown in Table 5, under 132 °C isothermal condition, the predicted maximum cell surface temperature is lower than that under 145 and 160 °C; and it took 140.05 min for the cell to reach its maximum temperature. This is much longer than the two isothermal conditions at higher temperatures.

In Fig. 10, the heat generation rates of different decomposition reactions are plotted against time. It can be observed that the temperature has considerable influence on the heat generation rates in $\dot{Q}_{Mix}$, the heat generation rate due to decomposition of electrolyte and other material as well as earlier combustion, being significantly affected. These results suggest that the significant change of the heat generation due to cathode and in $\dot{Q}_{Mix}$ from 131 to 132 °C is the main reason for the TR onset temperature to be between this range for the 21700 LIB considered in the present study. In fact, the predicted heat generation rates due to the cathode and in $\dot{Q}_{Mix}$ were almost zero for the 131 °C case with the corresponding curves collapsing to the horizontal axis.

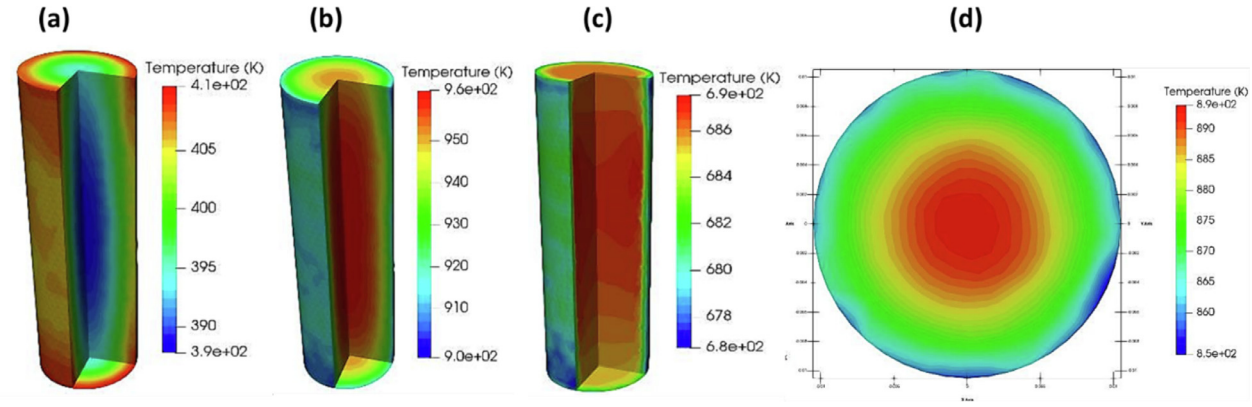

Fig. 15. The predicted temperature contours of the cell at different times (a) before TR, (b) during TR and (c) after TR during the cooling of the cell (d) Cross section of the cell.

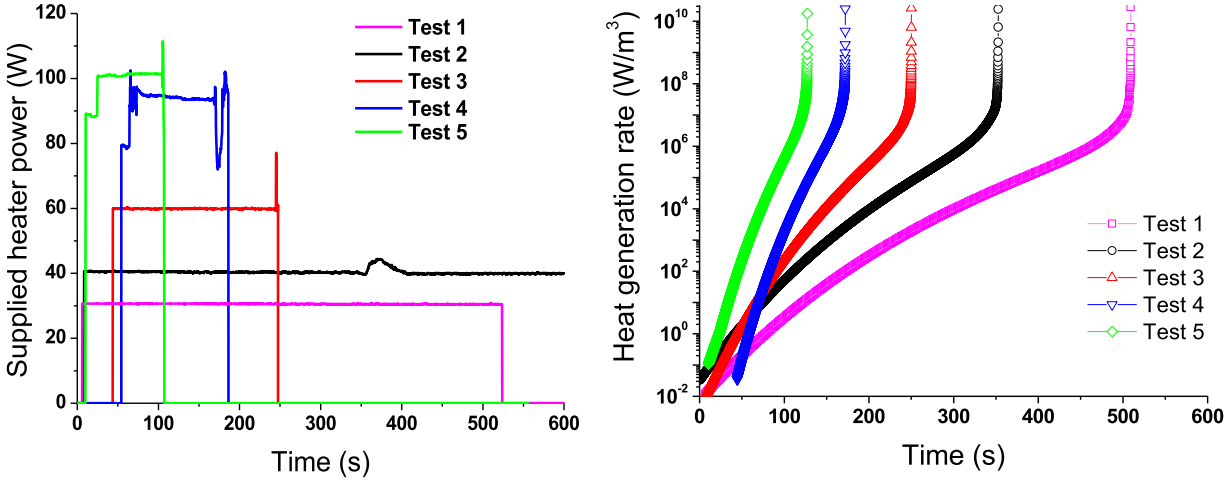

Fig. 16. The supplied heat power *vs* time (left)) and the predicted heat generation rate (right).

Table 6
Summary of the test configuration and Kanthal wire heaters.

Test No.	Initial cell temperature (°C)	Ambient temperature (°C)	Average heater power (W)	Heater duration (start time- stop time)
Test 1	19.2	-	30.66	6.2–523.6 s
Test 2	25.4	16.1	40.46	9.40 s- Continuous
Test 3	22.5	14.5	59.85	46.6–260.2 s
Test 4	26.2	11.5	92.144	54.4–186.2 s
Test 5	32.3	15.1	101.05	10.5–107 s

6. Measurements, validation and heat generation rates for tests with Kanthal wire heaters

6.1. Tests with Kanthal wire heaters and further validation

Laboratory tests were conducted for localized heating by electrical power of Kanthal wires using the LIB testing facility at the Science Divisions of the Health and Safety Executive (HSE) in the UK. A total of 6 turns (440 mm) of 0.35 mm diameter at defined power was used. Five tests with different initial and ambient temperatures were performed. The test conditions including the heating power and its duration are listed in Table 6. To study the changing patterns of cell surface temperature during evolution to TR under different initial temperatures and heater powers, they were deliberately kept. The change in the ambient temperature was, however, due to natural variation of the weather on the days when different tests were carried out. The heaters were turned on at different times and turned off following cell ignition. The power of the heater was kept mostly unchanged until it was turned off. These tests were named as soft-initiating tests as the heating rate was slower than that of patch heater under the same heater power as shown in Table 1 [20].

Fig. 11 depicts the setting of a heater in the computational model, which mimics the experimental arrangement, in which a layer of double-sided Kapton tape was added around the top of the cell as shown in Fig. 11(a). The Kanthal wire was wound around the cell from the 10 mm marking as shown in Fig. 11(b). Assuming an even spacing of 1 mm between the turns, the wire was wound around the cell. A layer of the single-sided Kapton tape was then added over the top of the wires to hold them in position, followed by a layer of 3M glass fibre insulating tape of 12 mm wide as shown in Fig. 11(c). The cells are kept vertical in the cell holder like in the EV-ARC tests. The cell surface temperature was monitored at the middle height on the side. After TR, a fan was switched on to vent the hot gases.

In the numerical model, the cell bottom was assumed to be thermally insulated. The other boundaries exchange heat with the surroundings through convection and radiation. The forced cooling

Table 7
Summary of the predictions and measurements for tests with Kanthal wire heaters.

Test No.	Max cell surface temperature (°C)		Relative error (%)	Time to max cell surface temperature (s)		Relative error (%)
	Measured	Predicted		Measured	Predicted	
Test 1	738.1	713.94	3.27	524.4	510	2.75
Test 2	655	668.19	-2.01	351.4	353.01	-0.46
Test 3	695	684.1	1.57	260.2	257.0	1.23
Test 4	807.5	638.72	20.90	171.2	173.02	-1.06
Test 5	717.4	558.14	22.20	107.0	127.0	-18.70

due to fan ventilation was neglected in the simulation due to unclear conditions for airflow around the cell. A total of 4200 tetrahedra cells were used in the 3-D model based on the mesh independence tests. Adaptive time step as mentioned previously was implemented to capture the relatively large temperature change in a small duration during the TR of the cell.

Fig. 12(a–e) shows the comparison between the predicted and measured cell surface temperatures in all five tests. In Test 2 shown in Fig. 12(b), continuous heating of 40 W was applied before and after TR. To examine the effect of supplied heat on the cell after TR, continuous heating was used in Test 2. During TR, the ejection of some jelly roll was observed in all the tests followed by the gradual decrease in the temperature due to heat dissipation to the surrounding. As Test 2 with continuous heating already showed that continuous heating had little effect on the cell surface temperature, it was felt there was no need to repeat the tests with the same condition without continuous heating. In other Tests (1, 3, 4 and 5), the heater power was turned off as soon as the cell entered TR. The model with the kinetic parameters derived from the EV-ARC HWS tests captures well the TR temperature and timing. The higher measured temperature in Fig. 12(d) (Test 4) may be caused by the engulfing flame. While Fig. 12(e) shows the lowest maximum TR temperature in Test 5, which had the highest heating power. This might be due to the shorter time to TR onset and much shorter duration of the heater, which was switched off after flaming.

The predictions agree well with the measurements for Tests 1, 2 and 3, which had constant/uniform heater power as shown in Fig. 12(a–c). In Tests 4 and 5, the relatively larger heater power led to charring and smoking of the adhesive securing the wire heater to the cell, adding further heat to the cell while the resulting additional temperature increase is not considered in the model and hence relatively larger discrepancies are found between the predicted and measured maximum cell surface temperatures for these two tests. The predicted temperatures during the evolution to TR were noted to be slightly larger than the measurements in almost all the cases. This was thought to be due to the gradually loosening of the contact between the cell surface and the thermocouples as shown in Fig. 13. After TR, relatively larger discrepancies were found between the predicted and measured cell surface temperatures. This was mainly because a fan was turned on to remove the ejected gases while the numerical simulations only considered natural convection as the fan speeds were not recorded. In addition, relatively looser contact between the thermocouple and the cell surface was also noted after TR and some thermocouples were observed to be falling from the surface of the ruptured cell.

Table 7 illustrates the predicted and measured times to maximum cell surface temperature are in excellent agreement with the largest discrepancy being less than 3% for Tests 1–4. The predicted and measured maximum cell surfaces temperatures differ by less than 3.5% for Tests 1–3. Relatively larger discrepancies of over 20% exist between the predicted and measured maximum cell surface temperatures in Test 4 and 5. This is thought to be likely caused by the burning of the adhesive in Tests 4 and 5 as discussed above. Comparing with Table 5 which shows the predictions and measurements of the isothermal conditions, it is seen that the typical time heating was required for the cell to enter TR in Kanthal wire heaters is much shorter than the highest isothermal condition tests 160 °C, which took 2460 s.

Fig. 14 analyses the predicted heat generation rates of the different exothermic decomposition reactions in Test 3. It is seen that the decompositions of SEI and anode follow similar patterns while the heat generation due to decompositions of the cathode and “Mix” increased sharply when the cell approaches it maximum temperature. This is in consistent with the predictions in Fig. 10 for the simulated isothermal EV-ARC environment. Although the predicted increase of the heat generation due to cathode decomposition appears to be more gradual while still rapid for the HWS EV-ARC tests in Fig. 7(d), this is mainly because the duration, i.e. the horizontal axis, is much longer in thousands minutes rather than seconds.

Fig. 15 shows the temperature distribution inside the cell before, during and after TR. The temperature inside the cell is higher than that on the cell surface until the cell temperature is the same as the ambient temperature. Although as discussed in Section 2.5, the quantity of the heat added to each control volume within the 3-D cell block was the same for each time step, the control volumes in the outer regions of cell block were affected more by the heat gain from the heater and heat loss to the surroundings, resulting in temperature gradients in the predictions shown in Fig. 15. Fig. 15(d) shows the radial distribution of the temperature inside the cell. Due to consideration of anisotropic thermal conductivity of the cell material a temperature difference of $\sim$ 50°K was observed in Fig. 15(d). The higher temperature inside the cell is thought to be because of the prevailing abuse reactions inside the cell. The cell surface temperature decreases after TR until it became the same as the ambient temperature.

6.2. Heat generation rate during different stages of the tests with Kanthal wire heaters

The comparison of the supplied heat power in all the soft-initiation tests is shown in Fig. 16(a). The supplied heater power was increased from Test 1 to 5. Except in Tests 2, the heater power was stopped once the cell went into TR in all other tests. In Tests 1, the duration of the heater power was the lowest and it took much longer to trigger TR. The predicted time evolution of the heat generation rates for the 5 tests in Fig. 16(b) show similar trends. The higher the heater power, the higher of the predicted heat generation rate from the abuse reactions, leading to higher temperature rising rate and shorted time to the onset of TR.

In Fig. 17, the predicted volumetric heat generation rates for the five tests are plotted against the volume averaged cell temperature. The cell volume was calculated directly from its diameter and height. The five tests show almost the same results. Although the changes in the heater power resulted variation in the heat generation rate *vs* time, the model predicts the same relationship between the heat generation rates and volume averaged cell temperature.

Table 8
Comparison of maximum cell surface temperature and its time.

Heater type	Heating Power (W)/ temperature (°C)	Time for maximum cell surface temperature	Maximum cell surface temperature (°C)
ARC	HWS	2685.15 min	798.85
		2618.38 min	741.42
		2804.29 min	755.10
ARC	Isotherm 145 °C	77.27 min	711.06
	Isotherm 160 °C	41.16 min	737.05
Kanthal wire	30.66 W	524.4 s	738.1
	40.46 0057	351.4 s	655
	59.85 W	260.2 s	695
	92.144 W	171.2 s	807.5
	101.05 W	107.0 s	717.4

Fig. 18 shows the predicted total heat generated in the entire event of TR in all the five tests. The contribution of the cathode and "Mix" (decomposition of electrolyte and other remaining materials inside the cell) decomposition reactions were dominant in all the tests in comparison to that from SEI and anode decomposition. As mentioned earlier, some part of $\dot{Q}_{Ele-plus}$ may also be due to the ignition of the released flammable gases and hence includes some heat generated from the early stage of the combustion. The results show that the supplied heater power has some influences on the duration of TR and the heat generation from the abuse reactions. The predicted total heat generated during the tests (~37.73–42.1 kJ), which were obtained by integrating the heat generated during the simulation were found to be smaller than that in the EV-ARC tests (~39.45–43.45 kJ as shown in Table 2). This small difference could be possibly caused by the ejection of hot gases and/or jelly roll materials, which led to reduction of the cell mass, its heat holding capacity and cell surface temperature. This factor was not considered in the simulation which assumed constant cell mass.

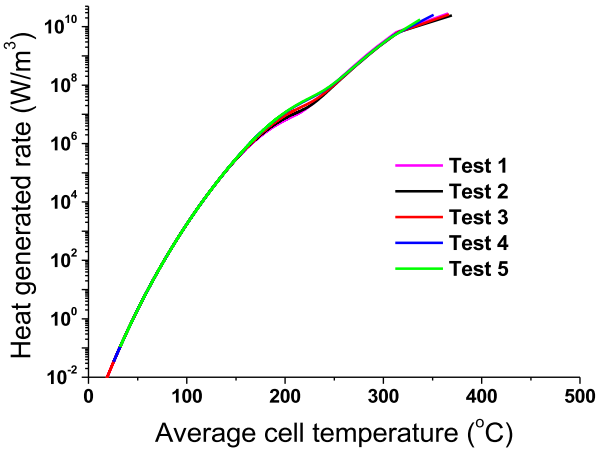

Fig. 17. Evolution of the heat generation rate in all 5 tests *vs* average cell temperature during TR evolution.

7. Influence of heater type and heating power on time to TR

The peak cell surface temperature and its time of occurrence are important parameters in hazard evaluation of LIBs. Table 8 shows the comparison of maximum cell surface temperature and its time. The same battery shows different TR characteristics under different heating methods for the same state of charge. The slow heating rates are observed in the cases with Kanthal wire heaters as 22–36% of the supplied electrical energy was lost to the ambient.

To further investigate the influence of the heater power and contact area between the heater and cell on TR evolutions, numerical simulations were conducted to predict the time to maximum cell surface temperature under thermal abuse by Kanthal wire and flexible patch heaters, keeping all other parameters the same. The patch heater has a 2″ by 2″ contact area with the cell surface as used in our previous study [20]. As shown in Fig. 19, the time to TR in case of the Kanthal heater is longer than that of the flexible patch heater. This was indeed the main reason why the heating by Kanthal heater was referred to as "soft-initiation heating method". It should also be mentioned that the 21700 cell considered in an earlier paper of our group [20] abused by the patch heater was a slightly different 21700 LIB with 5.0 Ah while the considered LIB in the present study was 4.8 Ah. In addition, the earlier tests were conducted in lower ambient temperatures and cell initial temperatures.

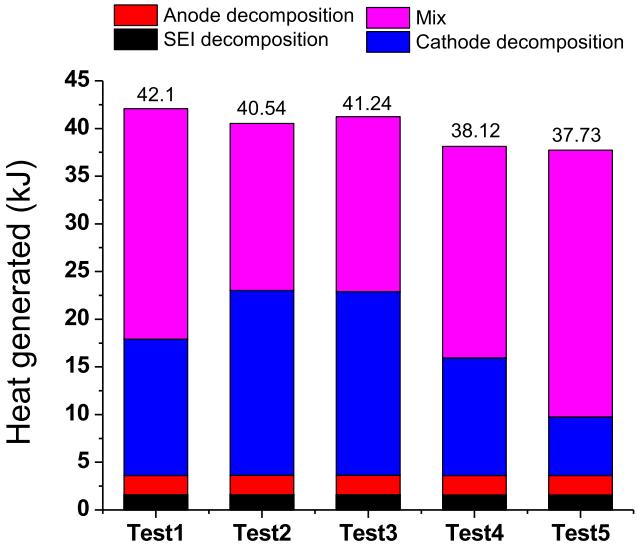

Fig. 18. The predicted heat generation of different abuse reactions during TR evolution in all the tests.

8. Effect of heat exchange with the surrounding and mitigation

Further, the heat exchange between the solid cell and surrounding air was examined by keeping all other parameters the same Test 1 with Kanthal wire heater. In the literature, heat exchange between the cell and the surrounding air has been treated as either natural convection [31–36] or forced convective cooling [37–39] with assumed constant convective heat transfer coefficient in Eq. (12). While it is theoretically possible to compute this directly by incorporating the air domain in the CFD analysis, it would significantly increase the computational time required. It

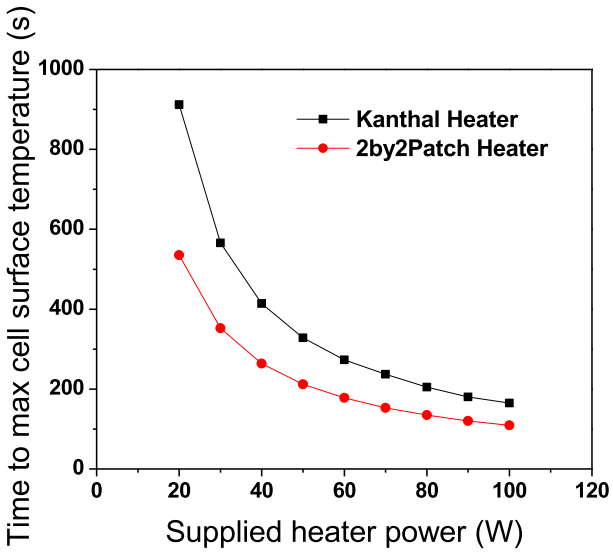

Fig. 19. Comparison of the predicted time to TR between the cases with heating abuse by Kanthal heater and flexible 2″ by 2″ patch heater.

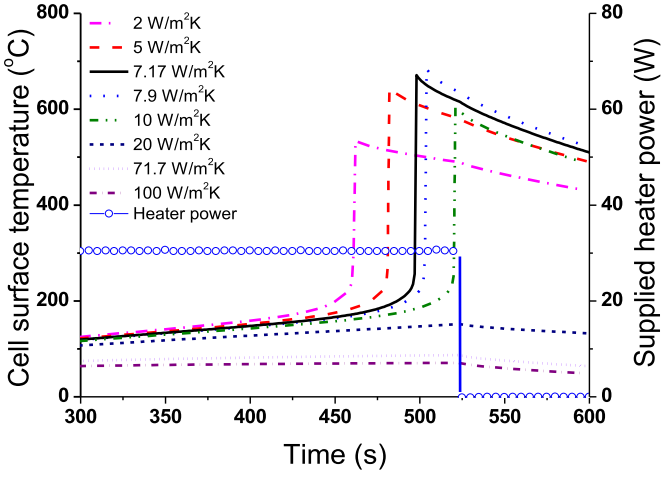

Fig. 20. Effect of convection heat transfer coefficient on the cell surface temperature.

was hence decided to conduct some parametric studies to evaluate the effect of variation in convective heat transfer coefficient.

A range of convective heat transfer coefficients were considered from previously used in the literature for natural convection, 2 W/m^{2}K [61], 5 W/m^{2}K [62,63], 7.17 W/m^{2}K [64], 7.9 W/m^{2}K [65], 10 W/m^{2}K [66,67] and forced convection, 20 W/m^{2}K [68], 71.7 W/m^{2}K [64] and 100 W/m^{2}K [69]. As shown in Fig. 20, the value of the convective heat transfer coefficient has considerable influences on the predicted cell surface temperature evolution. These results evidence the importance of heat dissipation from the heater and cell to the environment on TR evolution. The time to reach the maximum cell surface temperature increases with the increased of heat dissipation to the environment when larger heat transfer coefficient was used for natural convection. If the convective heat transfer coefficient was specified according to previously used values for forced cooling, the supplied heater power for the specified time would not trigger TR. This finding has important implication for battery thermal management and the mitigation effects, i.e. the use of forced convective cooling, whenever possible, would reduce the propensity to TR and improve safety.

9. Concluding remarks

An efficient 3-D modeling approach has also been developed and validated with the modified in-house version of OpenFOAM incorporating 3-D conduction within the cell as well as heat dissipation through convective and radiative heat transfer. Further numerical simulations have been conducted to fill the experimental gaps The following key findings can be drawn from the present study:

- It is viable to use EV-ARC derived kinetic parameters to predict TR behavior and heat generation induced by different thermal abuse in a CFD framework. The predicted temperature evolutions for isothermal abuse conditions agree well with the measurements with the largest discrepancy being less than 0.68%. Relatively larger discrepancies of 6.75% are found between the predicted and measured maximum cell surface temperatures.
- The TR onset temperature of the considered 21700 LIB in isothermal EV-ARC environment is predicted to be between 131 and 132 °C. But it would take more than two hours for TR to be induced under this temperature.
- In all considered scenarios for the present LIB, the predicted heat generation rate due to the decompositions of SEI and anode follow similar patterns while that from cathode and “Mix” increase sharply near the maximum cell surface temperature. This finding indicates the possibility of delaying TR onset temperature by optimising the cathode and electrolyte materials.
- The time to maximum cell temperature decreases rapidly with the increase of the heating power. Under 100 W Kanthal heating, for example, it takes less than 2 min to the cell to enter TR. It is hence of critical importance to prevent TR through efficient thermal management. While intervention/mitigation measures after the onset of combustion might help to reduce the resulting fire consequences, they are unlikely to be effective to prevent the propagation of the thermal runaway.
- Convective cooling on the cell surface has considerable influence on TR evolution. The use of forced convection, e.g. by fans, is an effective means to mitigate TR.

Finally, it should be mentioned that the present modeling approach, although developed and validated with tests for a specific type of 21700 LIB, the process of its development is generic and can be easily extended to other cell types.

Declaration of Competing Interest

The authors declare that they have no known competing financial interests or personal relationships that could have appeared to influence the work reported in this paper.

CRediT authorship contribution statement

Ashish V. Shelkea: Conceptualization, Methodology, Investigation, Visualization, Writing – original draft, Writing – review & editing. **Jonathan E.H. Buston:** Methodology, Writing – review & editing. **Jason Gill:** Methodology, Writing – review & editing. **Daniel Howard:** Methodology, Writing – review & editing. **Rhiannon C.E. Williams:** Methodology, Writing – review & editing. **Elliott Read:** Methodology, Writing – review & editing. **Ahmed Abaza:** Formal analysis, Methodology, Writing – review & editing. **Brian Cooper:** Formal analysis, Methodology, Writing – review & editing. **Philp Richards:** Formal analysis, Methodology, Writing – review & editing. **Jennifer X. Wen:** Conceptualization, Methodology, Supervision, Writing – review & editing.

Acknowledgments

The work is conducted within the frame of the "Lithium-Ion Battery Research In Safety (LIBRIS)" project funded by Innovate UK (Project No. 105296). Aspects of the work described in this paper were undertaken at the Health and Safety Executive (HSE) Science and Research Centre. Its contents, including any opinions and/or conclusions expressed, are those of the authors alone and do not necessarily reflect HSE policy.

References

[1] V. Ruiz, A. Pfrang, A. Kriston, N. Omar, P. Van den Bossche, L. Boon-Brett, A review of international abuse testing standards and regulations for lithium ion batteries in electric and hybrid electric vehicles, Renew. Sustain. Energy Rev. 81 (2018) 1427–1452.
[2] B. Diouf, R. Pode, Potential of lithium-ion batteries in renewable energy, Renew. Energy 76 (2015) 375–380.
[3] J.B. Quinn, T. Waldmann, K. Richter, M. Kasper, M. Wohlfahrt-Mehrens, Energy density of cylindrical Li-ion cells: a comparison of commercial 18650 to the 21700 cells, J. Electrochem. Soc. 165 (2018) A3284, doi:10.1149/2.0281814jes.
[4] T. Kang, S. Park, P.Y. Lee, I.H. Cho, K. Yoo, J. Kim, Thermal analysis of a parallel-configured battery pack (1S18P) using 21700 cells for a battery-powered train, Electronics 9 (2020) 1–12, doi:10.3390/electronics9030447.
[5] A. Relefors, Investigation and application of safety parameters for lithium-ion battery systems for application in battery management systems, Project Report, Chemical Science and Engineering, KTH ROYAL INSTITUTE OF TECHNOLOGY, Stockholm, Sweden (2020).
[6] R. Zhao, J. Liu, F. Ma, A comprehensive comparison of the phase change material-based internal and external cooling systems, ECS Meet. Abstr. (2020) 460 MA2020-01460, doi:10.1149/ma2020-012460mtgabs.
[7] L. Lao, Y. Su, Q. Zhang, S. Wu, Thermal runaway induced casing rupture: formation mechanism and effect on propagation in cylindrical lithium ion battery module, J. Electrochem. Soc. 167 (2020) 090519, doi:10.1149/1945-7111/ab8807.
[8] X. Hu, J. Jiang, D. Cao, B. Egardt, Battery health prognosis for electric vehicles using sample entropy and sparse Bayesian predictive modeling, IEEE Trans. Ind. Electron. 63 (2015) 2645–2656.
[9] C.Y. Wang, G. Zhang, S. Ge, T. Xu, Y. Ji, X.G. Yang, Y. Leng, Lithium-ion battery structure that self-heats at low temperatures, Nature 529 (2016) 515–518.
[10] H. Chen, J.E.H. Buston, J. Gill, D. Howard, R.C.E. Williams, C.M. Rao Vendra, A. Shelke, J.X. Wen, An experimental study on thermal runaway characteristics of lithium-ion batteries with high specific energy and prediction of heat release rate, J. Power Sources 472 (2020) 228585, doi:10.1016/j.jpowsour.2020.228585.
[11] A.R. Baird, E.J. Archibald, K.C. Marr, O.A. Ezekoye, Explosion hazards from lithium-ion battery vent gas, J. Power Sources 446 (2020), doi:10.1016/j.jpowsour.2019.227257.
[12] H. Niu, C. Chen, D. Ji, L. Li, Z. Li, Y. Liu, X. Huang, Thermal-runaway propagation over a linear cylindrical battery module, Fire Technol. (2020) 0–14, doi:10.1007/s10694-020-00976-0.
[13] H. Li, H. Chen, G. Zhong, Y. Wang, Q. Wang, Experimental study on thermal runaway risk of 18650 lithium ion battery under side-heating condition, J. Loss Prev. Process Ind. 61 (2019) 122–129, doi:10.1016/j.jlp.2019.06.012.
[14] S. Gao, L. Lu, M. Ouyang, Y. Duan, X. Zhu, C. Xu, B. Ng, N. Kamyab, R.E. White, P.T. Coman, Experimental study on module-to-module thermal runaway-propagation in a battery pack, J. Electrochem. Soc. 166 (2019) A2065–A2073, doi:10.1149/2.1011910jes.
[15] C. Lee, A.O. Said, S.I. Stoliarov, Passive mitigation of thermal runaway propagation in dense 18650 lithium ion cell assemblies, J. Electrochem. Soc. 167 (2020) 090524, doi:10.1149/1945-7111/ab8978.
[16] S. Gao, X. Feng, L. Lu, M. Ouyang, D. Ren, A test approach for evaluating the safety considering thermal runaway propagation within the battery pack, ECS Trans. 77 (2017) 225–236, doi:10.1149/07711.0225ecst.
[17] T. Liu, Y. Liu, X. Wang, X. Kong, G. Li, Cooling control of thermally-induced thermal runaway in 18,650 lithium ion battery with water mist, Energy Convers. Manag. 199 (2019) 111969, doi:10.1016/j.enconman.2019.111969.
[18] M. Chen, J. Liu, Y. He, R. Yuen, J. Wang, Study of the fire hazards of lithium-ion batteries at different pressures, Appl. Therm. Eng. 125 (2017) 1061–1074, doi:10.1016/j.applthermaleng.2017.06.131.
[19] C.F. Lopez, J.E. Soc, C.F. Lopez, J.A. Jeevarajan, P.P. Mukherjee, Experimental analysis of thermal runaway and propagation in lithium- ion battery modules experimental analysis of thermal runaway and propagation in lithium-ion battery modules, J. Electrochem. Soc. 162 (2015) A1905–A1915, doi:10.1149/2.0921509jes.
[20] H. Chen, J.E.H. Buston, J. Gill, D. Howard, R.C.E. Williams, E. Read, A. Abaza, B. Cooper, J.X. Wen, A simplified mathematical model for heating-induced thermal runaway of lithium-ion batteries, J. Electrochem. Soc. 168 (2021) 010502, doi:10.1149/1945-7111/abd64c.
[21] P.T. Coman, E.C. Darcy, C.T. Veje, R.E. White, Numerical analysis of heat propagation in a battery pack using a novel technology for triggering thermal runaway, Appl. Energy 203 (2017) 189–200, doi:10.1016/j.apenergy.2017.06.033.
[22] F. Larsson, B.E. Mellander, Abuse by external heating, overcharge and short circuiting of commercial lithium-ion battery cells, J. Electrochem. Soc. 161 (2014) A1611–A1617, doi:10.1149/2.0311410jes.
[23] A.W. Golubkov, D. Fuchs, J. Wagner, H. Wiltsche, C. Stangl, G. Fauler, G. Voitic, A. Thaler, V. Hacker, Thermal-runaway experiments on consumer Li-ion batteries with metal-oxide and olivin-type cathodes, RSC Adv. 4 (2014) 3633–3642, doi:10.1039/c3ra45748f.
[24] P. Peng, F. Jiang, Thermal behavior analyses of stacked prismatic $LiCoO_2$ lithium-ion batteries during oven tests, Int. J. Heat Mass Transf. 88 (2015) 411–423.
[25] B. Lei, W. Zhao, C. Ziebert, N. Uhlmann, M. Rohde, H.J. Seifert, Experimental analysis of thermal runaway in 18650 cylindrical Li-ion cells using an accelerating rate calorimeter, Batteries 3 (2017) 1–14, doi:10.3390/batteries3020014.
[26] C. Zhao, J. Sun, Q. Wang, Thermal runaway hazards investigation on 18650 lithium-ion battery using extended volume accelerating rate calorimeter, J. Energy Storage 28 (2020) 101232, doi:10.1016/j.est.2020.101232.
[27] X. Feng, M. Fang, X. He, M. Ouyang, L. Lu, H. Wang, M. Zhang, Thermal runaway features of large format prismatic lithium ion battery using extended volume accelerating rate calorimetry, J. Power Sources 255 (2014) 294–301, doi:10.1016/j.jpowsour.2014.01.005.
[28] P. Huang, P. Ping, K. Li, H. Chen, Q. Wang, J. Wen, J. Sun, Experimental and modeling analysis of thermal runaway propagation over the large format energy storage battery module with $Li_4Ti_5O_{12}$ anode, Appl. Energy 183 (2016) 659–673, doi:10.1016/j.apenergy.2016.08.160.
[29] M. Chen, D. Zhou, X. Chen, W. Zhang, J. Liu, R. Yuen, J. Wang, X. Chen, W. Zhang, J. Liu, R. Yuen, J. Wang, Investigation on the thermal hazards of 18650 lithium ion batteries by fire calorimeter, J. Therm. Anal. Calorim. 122 (2015) 755–763, doi:10.1007/s10973-015-4751-5.
[30] J. Anderson, F. Larsson, P. Andersson, B.E. Mellander, Thermal modeling of fire propagation in lithium-ion batteries, in: Proceedings of the 24th International Technical Conference on the Enhanced Safety of Vehicles, Gothenburg, Sweden, 2015, pp. 1–8. June 8-11, 2015.
[31] D.P. Finegan, M. Scheel, J.B. Robinson, B. Tjaden, I. Hunt, T.J. Mason, J. Millichamp, M. Di Michiel, G.J. Offer, G. Hinds, D.J.L. Brett, P.R. Shearing, In-operando high-speed tomography of lithium-ion batteries during thermal runaway, Nat. Commun. 6 (2015) 1–10, doi:10.1038/ncomms7924.
[32] M. Lammer, A. Königseder, V. Hacker, Holistic methodology for characterisation of the thermally induced failure of commercially available 18650 lithium ion cells, RSC Adv. 7 (2017) 24425–24429.
[33] X. Liu, S.I. Stoliarov, M. Denlinger, A. Masias, K. Snyder, Comprehensive calorimetry of the thermally-induced failure of a lithium ion battery, J. Power Sources 280 (2015) 516–525.
[34] X. Liu, Comprehensive Calorimetry and Modelling of the Thermally Induced Failure of a Lithium Ion Battery, University of Maryland, College Park, 2016.
[35] Z. Wang, J. Ma, L. Zhang, Finite element thermal model and simulation for a cylindrical Li-ion battery, IEEE Access 5 (2017) 15372–15379, doi:10.1109/ACCESS.2017.2723436.
[36] A. Kriston, A. Kersys, A. Antonelli, S. Ripplinger, S. Holmstrom, S. Trischler, H. Döring, A. Pfrang, Initiation of thermal runaway in Lithium-ion cells by inductive heating, J. Power Sources 454 (2020), doi:10.1016/j.jpowsour.2020.227914.
[37] C. Jin, Y. Sun, H. Wang, X. Lai, S. Wang, S. Chen, X. Rui, Y. Zheng, X. Feng, H. Wang, M. Ouyang, Model and experiments to investigate thermal runaway characterization of lithium-ion batteries induced by external heating method, J. Power Sources 504 (2021) 230065, doi:10.1016/j.jpowsour.2021.230065.
[38] X. Feng, X. He, M. Ouyang, L. Wang, L. Lu, D. Ren, S. Santhanagopalan, A coupled electrochemical-thermal failure model for predicting the thermal runaway behavior of lithium-ion batteries, J. Electrochem. Soc. 165 (2018) A3748–A3765, doi:10.1149/2.0311816jes.
[39] X.M. Xu, R.Z. Li, L. Zhao, D.H. Hu, J. Wang, Probing the thermal runaway triggering process within a lithium-ion battery cell with local heating, AIP Adv. 8 (2018), doi:10.1063/1.5039841.
[40] K. Shah, D. Chalise, A. Jain, Experimental and theoretical analysis of a method to predict thermal runaway in Li-ion cells, J. Power Sources 330 (2016) 167–174, doi:10.1016/j.jpowsour.2016.08.133.
[41] G.H.H. Kim, A. Pesaran, R. Spotnitz, A three-dimensional thermal abuse model for lithium-ion cells, J. Power Sources 170 (2007) 476–489, doi:10.1016/j.jpowsour.2007.04.018.
[42] P. Ping, Q. Wang, Y. Chung, J. Wen, Modelling electro-thermal response of lithium-ion batteries from normal to abuse conditions, Appl. Energy 205 (2017) 1327–1344, doi:10.1016/j.apenergy.2017.08.073.
[43] T.D. Hatchard, D.D. MacNeil, A. Basu, J.R. Dahn, Thermal model of cylindrical and prismatic lithium-ion cells, J. Electrochem. Soc. 148 (2001) A755, doi:10.1149/1.1377592.
[44] P.T. Coman, S. Rayman, R.E. White, A lumped model of venting during thermal runaway in a cylindrical lithium cobalt oxide lithium-ion cell, J. Power Sources 307 (2016) 56–62, doi:10.1016/j.jpowsour.2015.12.088.
[45] L. Ménard, G. Fontès, S. Astier, Dynamic energy model of a lithium-ion battery, Math. Comput. Simul. 81 (2010) 327–339.
[46] J. Reyes-Marambio, F. Moser, F. Gana, B. Severino, W.R. Calderón-Muñoz, R. Palma-Behnke, P.A. Estevez, M. Orchard, M. Cortés, A fractal time thermal model for predicting the surface temperature of air-cooled cylindrical Li-ion cells based on experimental measurements, J. Power Sources 306 (2016) 636–645.
[47] R. Spotnitz, J. Franklin, Abuse behavior of high-power, lithium-ion cells, J. Power Sources 113 (2003) 81–100.
[48] Q. Wang, P. Ping, X. Zhao, G. Chu, J. Sun, C. Chen, Thermal runaway caused fire and explosion of lithium ion battery, J. Power Sources 208 (2012) 210–224.

[49] L. Lu, X. Han, J. Li, J. Hua, M. Ouyang, A review on the key issues for lithium-ion battery management in electric vehicles, J. Power Sources 226 (2013) 272–288.
[50] P. Peng, F. Jiang, Thermal safety of lithium-ion batteries with various cathode materials: a numerical study, Int. J. Heat Mass Transf. 103 (2016) 1008–1016, doi:10.1016/j.ijheatmasstransfer.2016.07.088.
[51] C. Forgez, D.V. Do, G. Friedrich, M. Morcrette, C. Delacourt, D. Vinh Do, G. Friedrich, M. Morcrette, C. Delacourt, Thermal modeling of a cylindrical $LiFePO_4$/graphite lithium-ion battery, J. Power Sources 195 (2010) 2961–2968, doi:10.1016/j.jpowsour.2009.10.105.
[52] A. Greco, Numerical and analytical modelling of battery thermal management using passive cooling systems, PhD Thesis, Lancaster University, UK. (2015).
[53] S.C. Chen, Y.Y. Wang, C.C. Wan, Thermal analysis of spirally wound lithium batteries, J. Electrochem. Soc. 153 (2006) A637.
[54] M.N. Richard, J.R. Dahn, Accelerating rate calorimetry study on the thermal stability of lithium intercalated graphite in electrolyte. I. Experimental, J. Electrochem. Soc. 146 (1999) 2068.
[55] D. Ren, X. Liu, X. Feng, L. Lu, M. Ouyang, J. Li, X. He, Model-based thermal runaway prediction of lithium-ion batteries from kinetics analysis of cell components, Appl. Energy 228 (2018) 633–644, doi:10.1016/j.apenergy.2018.06.126.
[56] P.T. Coman, E.C. Darcy, C.T. Veje, R.E. White, Modelling li-ion cell thermal runaway triggered by an internal short circuit device using an efficiency factor and arrhenius formulations, J. Electrochem. Soc. 164 (2017) A587.
[57] D.D. MacNeil, D. Larcher, J.R. Dahn, Comparison of the reactivity of various carbon electrode materials with electrolyte at elevated temperature, J. Electrochem. Soc. 146 (1999) 3596.
[58] C.Y. Jhu, Y.W. Wang, C.M. Shu, J.C. Chang, H.C. Wu, Thermal explosion hazards on 18650 lithium ion batteries with a VSP2 adiabatic calorimeter, J. Hazard. Mater. 192 (2011) 99–107.
[59] C.Y. Jhu, Y.W. Wang, C.Y. Wen, C.M. Shu, Thermal runaway potential of $LiCoO_2$ and Li $(Ni_{1/3}Co_{1/3}Mn_{1/3})$ O_2 batteries determined with adiabatic calorimetry methodology, Appl. Energy 100 (2012) 127–131.
[60] D.D. MacNeil, J.R. Dahn, Test of reaction kinetics using both differential scanning and accelerating rate calorimetries as applied to the reaction of Li_xCoO_2 in non-aqueous electrolyte, J. Phys. Chem. A 105 (2001) 4430–4439.
[61] W. Zhao, G. Luo, C.Y. Wang, Modeling nail penetration process in large-format Li-ion cells, J. Electrochem. Soc. 162 (2014) A207, doi:10.1149/2.1071501jes.
[62] X. Feng, C. Weng, M. Ouyang, J. Sun, Online internal short circuit detection for a large format lithium ion battery, Appl. Energy 161 (2016) 168–180, doi:10.1016/j.apenergy.2015.10.019.
[63] A. Kurzawski, L. Torres-Castro, R. Shurtz, J. Lamb, J.C. Hewson, Predicting cell-to-cell failure propagation and limits of propagation in lithium-ion cell stacks, Proc. Combust. Inst. 0 (2020) 1–9, doi:10.1016/j.proci.2020.06.270.
[64] K.C. Chiu, C.H. Lin, S.F. Yeh, Y.H. Lin, K.C. Chen, An electrochemical modeling of lithium-ion battery nail penetration, J. Power Sources 251 (2014) 254–263, doi:10.1016/j.jpowsour.2013.11.069.
[65] R. Zhao, J. Liu, J. Gu, Simulation and experimental study on lithium ion battery short circuit, Appl. Energy 173 (2016) 29–39, doi:10.1016/j.apenergy.2016.04.016.
[66] L. Cai, R.E. White, Mathematical modeling of a lithium ion battery with thermal effects in COMSOL Inc. Multiphysics (MP) software, J. Power Sources 196 (2011) 5985–5989, doi:10.1016/j.jpowsour.2011.03.017.
[67] B. Mao, P. Huang, H. Chen, Q. Wang, J. Sun, Self-heating reaction and thermal runaway criticality of the lithium ion battery, Int. J. Heat Mass Transf. 149 (2020) 119178, doi:10.1016/j.ijheatmasstransfer.2019.119178.
[68] P. Huang, H. Chen, A. Verma, Q. Wang, P. Mukherjee, J. Sun, Non-dimensional analysis of the criticality of Li-ion battery thermal runaway behavior, J. Hazard. Mater. 369 (2019) 268–278, doi:10.1016/j.jhazmat.2019.01.049.
[69] R.M. Spotnitz, J. Weaver, G. Yeduvaka, D.H. Doughty, E.P. Roth, Simulation of abuse tolerance of lithium-ion battery packs, J. Power Sources 163 (2007) 1080–1086, doi:10.1016/j.jpowsour.2006.10.013.